An Anthropomorphic Robotic Finger With Innate Human-Finger-Like Biomechanical Advantages Part I: Design, Ligamentous Joint, and Extensor Mechanism

Yiming Zhu, Guowu Wei, *Member, IEEE*, Lei Ren, *Member, IEEE*, Zirong Luo, and Jianzhong Shang

***Abstract*—Exploring human hand fundamental biomechanical features and exploiting them to robotic hands have been proven to be an effective approach to enhancing artificial hands' performance, especially when interacting with various objects in dynamic unstructured environments. In this article, a bioinspired anthropomorphic robotic finger is first proposed, which embeds human finger musculoskeletal features in the design. Based on this design, three human-finger-like biomechanical advantages are systematically investigated and embodied in the bioinspired robotic finger. This article for the first time derives, presents, and experimentally verifies the mathematical models for the variable stiffness of finger ligamentous joints and self-adaptive morphing mechanism of finger flexible tendon sheaths, and validates and compares the influence of the reticular and linear extensor morphologies on fingertip feasible forces in three-dimensional (3-D) space. In this Part I of the article, two of the biomechanical properties, i.e., joint stiffness generated by the ligamentous joint of the finger, and fingertip feasible force space influenced by the reticular extensor mechanism are systematically investigated through theoretical modeling and experimental verification. Correspondingly, two biomechanical advantages were found, i.e., the ligamentous joint of the finger could provide anisotropic variable joint stiffness, enhancing the adaptivity, dexterity, and stability of fingers; and a reticular extensor mechanism could enlarge the fingertip feasible force space in 3-D space by 30.9% theoretically and 146.4% experimentally on average compared with the linear extensor, contributing to enrich force conditions during interactions. The third biomechanical advantage, i.e., fingertip force–velocity workspace can be augmented through the flexible tendon sheath, and grasping tests for a robotic hand designed with the aforementioned advantages are presented in Part II of this article.**

***Index Terms*—Bioinspired robotic finger, extensor mechanism, feasible force space, robotic hand, soft-rigid-hybrid design, variable joint stiffness.**

Manuscript received 19 May 2022; accepted 16 July 2022. Date of publication 5 September 2022; date of current version 8 February 2023. This work was supported in part by the Project of National Key R&D Program of China under Grant 2018YFC2001300 and in part by the Project of National Natural Science Foundation of China under Grant 91948302, Grant 91848204, Grant 52005209, and Grant 51675222. This paper was recommended for publication by Associate Editor F. Ficuciello and Editor E. Yoshida upon evaluation of the reviewers' comments. *(Corresponding authors: Guowu Wei; Lei Ren.)*

Yiming Zhu is with the School of Mechanical and Aerospace and Civil Engineering, University of Manchester, M13 9PL Manchester, U.K., and also with the College of Intelligence Science and Technology, National University of Defense Technology, 410073 Changsha, China (e-mail: yiming.zhu@manchester.ac.uk).

Guowu Wei is with the School of Science, Engineering, and Environment, University of Salford, M5 4WT Salford, U.K. (e-mail: g.wei@salford.ac.uk).

Lei Ren is with the School of Mechanical, Aerospace, and Civil Engineering, University of Manchester, M13 9PL Manchester, U.K., and also with the Key Laboratory of Bionic Engineering and Ministry of Education, Jilin University, Changchun 130012, China (e-mail: lei.ren@manchester.ac.uk).

Zirong Luo and Jianzhong Shang are with the College of Intelligence Science and Technology, National University of Defense Technology, 410073 Changsha, China (e-mail: luozirong@nudt.edu.cn; jz_shang_nudt@163.com).

Color versions of one or more figures in this article are available at https://doi.org/10.1109/TRO.2022.3200006.

Digital Object Identifier 10.1109/TRO.2022.3200006

I. Introduction

THE human hand, as a primary effector organ for our daily activities, is an excellent source that inspires the design and development of robotic hands. The intrinsic advanced dexterity and versatility of our hands make them able to accomplish various daily activities with ease. In fact, the excellent performance of a human hand is a result of the combined actions of the neural control, perception, and biomechanical properties of the hand itself. However, how each functional system acts and exerts an effect on the performance of the human hand is still not fully understood.

In addition to biological nerves and mechanoreceptors, the hand musculoskeletal system provides innate and ingenious biomechanical advantages for hand functions. This has been widely investigated and discussed by researchers in the field of biomechanics. Through biomechanical and cadaveric studies on human hands, Chao et al. [1] systematically explored the interesting properties of finger joints, including joint laxity and stiffness. Valero-Cuevas et al. [2], [3] discussed the force regulation function influenced by the quantity and morphologies of the flexor and extensor tendons, especially the complex reticular extensor mechanism. Brand and Hollister [4] investigated hand functions from the surgery point of view. Researchers in the field of robotics have realized and agreed that the ideas from biology and biomechanics of the human hand can benefit the design of the robotic hand [5], [6]. Thus, some bioinspired robotic hands have been developed in the past decade [7], [8]. But how to effectively introduce these biological mechanisms into the design of a robotic hand? And how to verify that these biomechanical properties can improve the performance of a robotic hand? preliminary attempts have been made [8], [9],

[10], but there is still no systematic theoretical or experimental investigation to tackle these questions.

To answer these questions, from the robotics research point of view, this article explores the intrinsic biomechanical advantages embedded in a bioinspired robotic finger with human-finger-like structures. In the proposed robotic finger, the capsuloligamentous joints, the tendinous networks of the extensor mechanisms, and the flexible tendon sheaths approximately duplicate the properties of their counterparts in a human finger. Based on the prototype, this article for the first time derives, presents, and experimentally verifies the mathematical models for the variable stiffness of finger ligamentous joints and the self-adaptive morphing mechanism of finger flexible tendon sheaths, and validates and compares the influence of the reticular and linear extensor morphologies on fingertip feasible forces in three-dimensional (3-D) space. In this Part I of the article, two of the biomechanical properties, i.e., joint stiffness generated by the ligamentous joint of the finger and fingertip feasible force space influenced by the reticular extensor mechanism, are systematically investigated through theoretical modeling and experimental verification.

It is found that with these two biomimetic structures, the performance of a robotic finger can be significantly improved.

1) The ligamentous structures of the joint can bring variable joint stiffness in both flexion–extension and abduction–adduction directions due to the innate deformation and material properties of the ligaments.
2) The reticular extensor mechanism can help enlarge the fingertip feasible force space by rerouting the propagation of tensions in the reticular extensor structure.

This research provides new insights into better robotic finger/hand design from the view of fundamental biomechanics.

II. Related Work

Researchers have been trying to explore the fundamental biological principles behind the excellent performance of human hands. Some unique biomechanical properties in the musculoskeletal system of human hands, including the ligamentous joints and extensor mechanisms, have been investigated through cadaveric tests and computational simulations. Some attempts have been made in bioinspired robotic hand design and development.

A. Joint Stiffness and Ligamentous Joints

Joint stiffness influences joint flexibility and stability. In human fingers, the capsuloligamentous structures and muscle–tendon units provide the constraint forces for the joint stiffness [1]. We commonly refer to the joint stiffness caused by the active isometric contraction of the muscle–tendon units as the active joint stiffness, and the one caused by the passive deformation of muscle–tendon units and capsuloligamentous structures as the passive joint stiffness [11], [12]. For the passive joint stiffness, the muscle–tendon units provide less than 50% of the contribution, and the capsuloligamentous structures play the dominant role [13]. Chao et al. [1] made a detailed investigation on the roles of capsuloligamentous structures, especially the collateral ligaments, on the MCP joint stiffness and stability through cadaveric tests. They found that the dorsal portions of both collateral ligaments provided the main restraints in joint flexion, and the joint stiffness varied in all the translational and rotational displacements. Similar results were found in [14] with more tests on cadaveric hand specimens and in [15] through an in-vivo study. To further study the deformation of the collateral ligaments in the MCP joint, a 3-D model of the MCP joint was created by Kataoka et al. [16], and the changes in the shape and length of each ligament portion during flexion were calculated. In fact, the joint stiffness is mostly influenced by the unique load-deformation property of the ligaments during motion. For instance, the low joint stiffness on straightening the finger can maintain good dexterity, and the high joint stiffness upon fully flexing the finger can relieve the intrinsic muscles fatigue by helping resist the lateral force when pulling a rope or pinching a key [17]. However, this kind of floating ligamentous joint design has hardly been very well presented and demonstrated in the robotic finger design. Xu and Todorov [18] designed a robotic hand with ligaments-articulated fingers. They used artificial crocheted ligaments to partially replicate the ligamentous structure, but the ligaments were designed in a linear shape rather than the actual band shape. Rubber-like materials have been widely used as ligaments on some recent biomimetic robotic hands [8], [9], [10]. However, this kind of material could not embody similar properties to human-hand ligaments because the microstructure of rubber is isotropic but that of the human ligament is anisotropic. In this article, the ligamentous joint structure is meticulously recreated in the robotic finger. And the corresponding joint stiffness is characterized systematically through theoretical modeling and experimental analysis.

B. Endpoint Feasible Force Set (Space) and Extensor Mechanism

The concept of "feasible force set" was proposed to mathematically describe the maximum force the fingertip could generate in every direction in the 3-D space. And all the possible linear combinations of these force vectors form the "feasible force set," defining the mechanical properties such as versatility and feasibility of a finger [19], [20]. Based on this, Inouye et al. [21] associated the feasible force set with the hand manipulation performance. The feasible force set henceforth became one of the main evaluation metrics for robotic hands or fingers [22]. It was also used to demonstrate the functional effect of the human hands' tendon routing distribution and the complex reticular extensor mechanism [23], [24].

Valero-Cuevas [2], [25] provided the background to explore the influence of the extensor mechanism on the fingertip force. A computational model group was developed to simulate the topology of the extensor mechanism based on the model of Winslow's tendinous rhombus for exploring the tension distribution in the structure [26]. Subsequently, making use of the model, the impact on the feasible force set produced by the extensor mechanism was investigated. The results indicated that this network structure could regulate the tensions propagating to the finger joint and thus enable the finger to generate various fingertip forces [23]. To better illustrate the

effect of the extensor mechanism on the fingertip force, two computational musculoskeletal models with reticular extensor and linear extensor were built by Synek and Pahr [24], leading to a result that the average forces produced by the reticular extensor were considerably larger. However, the research remained in the 2-D case and in the computational simulation study. With the morphological advantage of the extensor mechanism gradually revealed, it was increasingly used in robotic hands to simplify the control architecture and achieve better performance [18], [27], [28]. In these designs, the extensor mechanisms were fabricated by nylon strings, high-density polyethylene strings, or rubber sheets. However, despite a number of application instances of the extensor mechanism, there was no quantitative evaluation to characterize the effect of this structure on the behavior of robotic hands, especially on the fingertip feasible force space. This article aims to fill these gaps and present a detailed study on the biomechanical functions of the extensor mechanism in a finger through mathematical modeling and experimental verification.

C. Bioinspired Design of Robotic Hands

To advance the understanding of the aforementioned biomechanical and physiological mechanisms, as well as reproduce such mechanisms in robots, a number of physical prototypes of bioinspired robotic hands have been built in the past few decades [29].

In the early stage, the biological characteristics applied in the robotic hands were mostly embodied in the appearance and the whole musculoskeletal morphology, such as the number of the fingers, the degrees of freedom of the joints, and the tendon-driven actuation method. Such robotic hands include, to mention but a few, the Utah/MIT Hand [30], the Belgrade/USC Hand [31], the Southampton Hand [32], the Gifu hand III [33], the Cyber hand [34], the DLR/HIT Hand II [35], the Robonaut hand II [36], the Shadow Hand [37], and the ACT Hand [7]. Their bodies were completely rigid, and they all used the hinge joint design, which limited their adaptivity to different objects and external environments. One way to compensate for the disadvantages of rigid hinge joints is to use smart mechanism design, such as the metamorphic robotic hand [38], [39], [68], [69].

To further improve the adaptivity, soft materials were introduced to the robotic hand designs, such as the RBO Hand 2 with a soft body [40], the UB Hand 3 [41], and the Open Bionics Hand [42] with elastic joints, and the Awiwi Hand with elastic components in the actuation system [17]. The passive behavior of the soft materials improves the grasping quality but at the expense of manipulation performance and load capacity.

In recent years, a growing number of highly biomimetic robotic hands embedded with more human-hand-like features have been proposed. A highly bionic robotic hand with ligaments-articulated joints, reticular extensors, and elastic tendon sheaths was designed by Xu and Todorov [18]. This robotic hand could perform various grasping types through data glove control. To investigate human manipulation capability, Chepisheva et al. [9] developed a biologically inspired robotic hand that could operate chopsticks. The HR-hand developed by Faudzi et al. [43] was actuated by thin-soft muscles, whose performance was validated by comparing its motion trajectory to a cadaver model. Furthermore, to investigate the impact of the passive behavior of human hands, a 3-D printed anthropomorphic soft skeleton hand with flexible capsular joints was developed and used to study the dynamic behaviors and interactions in piano operation [8]. Recently, based on 3-D printing technology, Tebyani et al. [10] proposed a biomimetic cable-driven robotic finger by synthesizing the bones, ligaments, and visco-elastic tendons as a single part through a multimaterial 3-D printer, providing a new approach for robotic hand design, fabrication, and assembly.

The present research is based on a highly biomimetic robotic finger that is designed by embedding several properties of the musculoskeletal structure of human fingers, including the aforementioned three biomechanical advantages.

In terms of the structure design, different from other anthropomorphic robotic hands, polyethylene terephthalate (PET) braided fibers with a band shape were used for the ligaments in the proposed robotic finger rather than using the linear-shape fishing lines or rubberlike materials. Besides, the silicone-rubber-made capsules with wrinkles were used as the joint capsules to provide additional joint stability. We also designed some low-friction tendon sheath tunnels for each branch of the extensor mechanism to improve the transmission efficiency. In addition, rather than the rigid tendon sheath, in our design, the silicone-rubber-made tendon sheath membrane and the embedded PTFE tubes constitute the flexible tendon sheaths with smooth tunnels inside. Overall, compared with the fingers of other robotic hands, the adopted structures and materials are expected to empower our robotic fingers with more human-finger-like properties and enhanced functional performance, such as grasping. Moreover, the mathematical model of the ligamentous joint proposed in Part I of the article paves the way to analyze the properties of this type of joint. And the comparative method used in studying the reticular extensor could better illustrate the impact of this structure on the robotic finger performance. These two biomechanical advantages were first investigated and verified based on a highly biomimetic robotic finger, providing an effective approach to exploring the properties of human-finger-like structures.

III. Finger Anatomy and Bioinspired Design

The notion of the robotic finger design was derived from the anatomical structures and biomechanics of the human finger. Many unique advantages can be found in human fingers, which extensively benefit from the soft tissues and special functional structures. Inspiring from this, we developed a multilayer anthropomorphic robotic finger to reconstruct the structures of the human finger to embody the human-finger-like advantages.

Fig. 1 shows a cadaveric human finger structure and the multilayer design of an anthropomorphic robotic index finger. It can be seen that, except for the skin, there are mainly six structural components forming three layers. The first or the base layer includes the bones and the articular cartilage. The second layer has the joint ligaments and the joint capsule. And the third layer includes the tendons and the tendon sheaths. These six

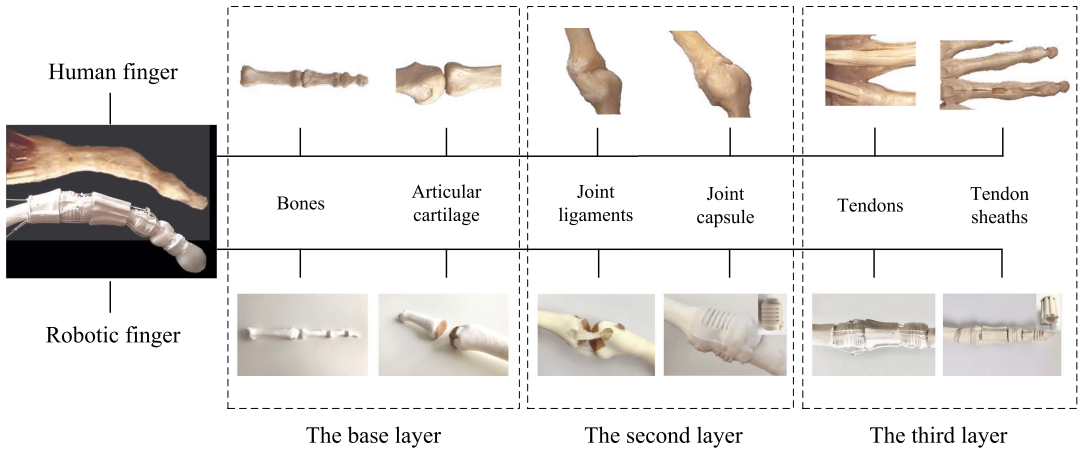

Fig. 1. Multilayer structure of a human and robotic finger. The base layer contains bones and the articular cartilage, the second layer comprises the joint ligaments and the joint capsules, and the third layer consists of tendons and tendon sheaths.

main components in the finger have their individual features and functions, which are addressed in detail in this section.

A. Base Layer—Phalanges and Articular Cartilage

The phalanges and the articular cartilage form the base layer of a finger, in which the phalanges are the only rigid components in the whole finger. The three phalanges and one metacarpal bone make up the three finger joints, namely, the distal interphalangeal (DIP) joint, the proximal interphalangeal (PIP) joint, and the metacarpophalangeal (MCP) joint. These phalanges need to be strong and stiff enough as they play an essential role in bearing external loads. Besides, the palmar surface of each phalanx shaft is slightly longitudinally concave to accommodate the muscles or tendons [44]. The palmar surface of the joint is convex to push the flexor tendons out to provide an initial flexion moment arm, avoiding actuation difficulty at the initial motion stage. Moreover, the unique shape of the biological joint articulation would exert a significant influence on the joint motion, which can be seen from different motion degrees of freedom in the DIP, PIP, and MCP joints. Therefore, preserving the intact shape of the phalanges and ensuring the material strength are the major concerns in the design.

In the proposed robotic finger, the bone models came from the CT scanning data of a 23-year-old healthy male [45], which was then processed in the software Mimics Research 19.0 [see Fig. 2(a)]. After that, the computer-aided design (CAD) model [see Fig. 2(c)] of the bones was generated and subsequently imported into the software SolidWorks, where the fixture holes of the ligaments' origins and insertions were located based on the MR images [see Fig. 2(b)] and the cadaver data from previous research [1]. The modified bone models were then 3-D printed with the 405-nm UV white photopolymer resin by using the Anycubic Photon S LCD-based SLA 3-D printer, and the printed physical model is shown in Fig. 2(d).

Covering the finger joint surface is a thin, dense, smooth, connective tissue, namely articular cartilage, minimizing the friction and wear in the relative movement of adjacent joint surfaces. The water occupies nearly 80% of the articular surface, controlling the joint lubrication. And the collagen fibrils and the proteoglycans make up the structural networks to support the internal mechanical stresses [46]. Thus, the articular cartilage can be simply regarded as a two-layer structure, including a lubrication layer and a structural supporting layer [47].

In the cartilage design of the proposed finger, the 0.13-mm-thick flexible polytetrafluoroethylene (PTFE) adhesive tape is firmly stuck onto the bones' ends to act as the articular cartilage, as shown in Fig. 2(d). It is structured by PTFE-coated woven fiberglass fabric, of which the PTFE layer could offer a low friction and nonstick surface without leaving residues, and the underneath fiberglass provides enough strength and structural stability.

B. Second Layer—Capsuloligamentous Structure

The second layer of the finger is the capsuloligamentous structure, including the joint ligaments and the joint capsules. There are mainly three ligaments around a joint bonding two adjacent phalanges together, including two collateral ligaments and one palmar or volar plate.

The biomechanical property of the ligament is associated with its microstructure. For example, it has a characteristic sinusoidal wave pattern that is known as crimp [48]. Once a load is initially applied to a ligament, the "crimp pattern" will be straightened without causing much tension. This stage can be defined as the toe region. As the loading continues, the stiffness of the ligament increases sharply, resulting in elastic deformation. This region is called the elastic or linear region, followed by yielding and failing of the structure in the end [46].

In the proposed design, polyethylene terephthalate (Polyester, PET) fiber ribbons were selected to act as artificial ligaments and were sintered onto the bones. Its braided structure closely resembles the crimp pattern of human ligaments, providing an analogous strain–stress property. Moreover, the band shape allows its different portions to be stretched successively through the whole motion range to properly constrain the joint position and stiffness. Fig. 2(e) compares the human ligament and the PET ligament in different tension states.

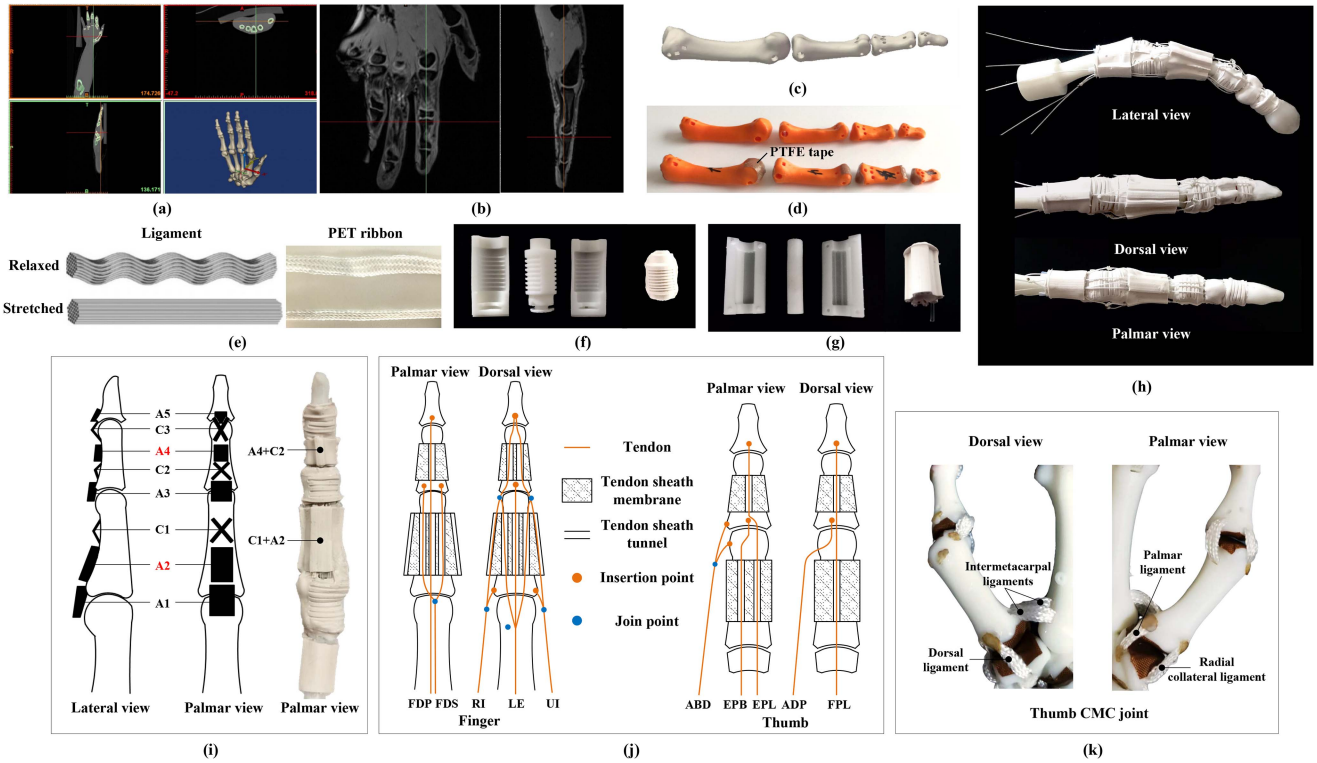

Fig. 2. Design and development of the robotic finger. (a) CT images of human hand bones. (b) MR images of human hand soft tissues. (c) CAD model of human finger bones. (d) 3-D printed physical model of robotic finger bones with PTFE articular cartilage. (e) "Crimp pattern" of the human ligament and the PET ribbon. (f) Designed molds and silicone rubber joint capsule. (g) Designed molds and silicone rubber tendon sheath with PTFE tubing. (h) Robotic finger model with tendons. (i) Distribution of the tendon sheaths along the human and robotic finger. (j) Schematic diagram of tendons' routing through tendon sheaths along the finger and the thumb. (k) Ligaments' distribution around the CMC joint of the robotic thumb model.

Furthermore, attached to the whole circumference of the articular end is a joint capsule that consists of an outer fibrous membrane and an inner synovial membrane. Together with the ligaments, it can properly limit the range of finger joint motion and prevent excessive laxity to assist joint stabilization. Meanwhile, it seals the synovial fluid inside that can provide a good lubrication condition [49], [50]. Additionally, there are some folds on capsules' surface, allowing a sufficient range of motion when stretched and simultaneously preventing accumulation hump when compressed. The joint capsule in the proposed design has no liquid inside, and it only plays the role of assisting the joint stabilization. Several customized molds were designed and 3-D printed. The liquid silicone rubber (Polycraft GP3496-F Shore A13) was injected into the molds and cured into a 0.5-mm-thick elastic capsule with triangle-shaped folds on the dorsal-palmar sides to reduce the resistance moment and structural accumulation during flexion, as shown in Fig. 2(f).

C. Third Layer—Tendons and Tendon Sheaths

The tendons and tendon sheaths together constitute the finger's third layer. Along the finger, there are mainly two flexor tendons that are the flexor digitorum superficialis (FDS) and the flexor digitorum profundus (FDP), and one extensor mechanism covering the dorsal side of the finger whose proximal ends connect with the long extensor (LE), the ulnar interosseous (UI), the radial interosseous (RI), and the lumbrical muscle (LU). For the index finger, another tendon, called extensor indicis, spreads out from the extensor mechanism, enhancing the independent control of the index finger [51]. It is noteworthy that the reticular extensor mechanism could provide the function of not only an extensor but also a flexor, abductor, adductor, or rotator according to the finger's targeting motion [27].

In the design, according to the abstracted Winslow's tendinous rhombus model [52] of the extensor mechanism, we fabricated a tendon network by using 30 lb fishing lines with a diameter of 0.43 mm made from 100% polyester Dacron fibres (Troutcatchers, U.K.), where the connective soft tissues were represented by silicone rubber tendon sheaths membrane. Through several assistive holes, the tendons can be firmly tied onto the bones. Because of the similarity in the locations and functions between the lumbrical muscle and the intrinsic muscle, the LU was removed in this design to simplify the actuation and control system. The physical prototype with tendons is shown in Fig. 2(h).

Furthermore, wrapping around the tendon is the tendon sheath. It is a two-layer membrane that consists of an inner synovial sheath layer and an outer fibrous sheath layer, allowing the tendon to move smoothly inside. The tendon sheaths along the palmar side of the phalanges form a pulley system that can guide the route of the flexor tendons and restrain their bowstringing behaviors by keeping them close to the joints [53]. Fig. 2(i) shows the schematic drawings of the components of the digital flexor tendon sheath. As can be seen, there are five annular strong pulleys (A1, A2, A3, A4, A5) and three thin,

pliable cruciate pulleys (C1, C2, C3) [54], [55]. Pulleys A2 and A4 have a significant influence on the moment arms of the flexor tendons, which could alter the biomechanical properties of the finger joints [44].

The flexible tendon sheaths were also molded with silicone rubber, as shown in Fig. 2(g). Inside the tendon sheaths, flexible PTFE tubes of 1.58-mm inner diameter (Adtech Polymer Engineering, Ltd., U.K.) were inserted to provide lubricated tunnels for the tendons. Ultimately, as can be seen in Fig. 2(i), the tendon sheaths cover around the middle, proximal, and metacarpal phalanges. To clearly show the tendon's morphology and how the tendon routes through the tendon sheaths, Fig. 2(j) presents the routing pathway schematic of all the tendons.

Additionally, the robotic thumb was developed based on the similar design and manufacturing approach. There are three joints in the thumb, including the interphalangeal (IP) joint, the MCP joint, and the first carpometacarpal (CMC) joint. The IP and MCP joints are very similar to those in the fingers. However, the structure of the CMC joint is much more complex, leading to higher dexterity and a larger motion range compared with other finger joints. First of all, the CMC joint has a biconcavoconvex saddle shape to form two rotation axes, allowing flexion and extension, abduction and adduction, and eventually circumduction [56]. Besides, the accurate number of the ligaments around the CMC joint has not been clearly identified. A widely accepted result is that there are seven principle ligaments in the CMC joint, which were demonstrated by Bettinger et al. [57], Nanno et al. [58], Ladd et al. [59], and Komatsu et al. [56]. They include three dorsal ligaments, two palmar ligaments, and two intermetacarpal ligaments. Among them, the palmar ligaments that are called the anterior oblique ligaments play the most important role in stabilizing the CMC joint. The dorsal ligaments are the strongest and stiffest ligaments, which help avoid dorsal dislocation and stabilize the joint, especially in power pinch and power grip [56], [58]. And the intermetacarpal ligaments can bring additional stability to the joint. Considering their similar roles of the ligaments on the same side, the CMC joint of the proposed robotic thumb has one palmar ligament, one dorsal ligament, and two intermetacarpal ligaments. Moreover, on the radial side, the human thumb CMC joint has the abductor pollicis longus (APL) tendon to help stabilization. Thus, we added one radial collateral ligament in the proposed design. And finally, there are a total of five ligaments around the CMC joint of the proposed thumb model, as shown in Fig. 2(k). To realize the dexterous motion, there are four extrinsic muscles [flexor pollicis longus (FPL), extensor pollicis longus (EPL), extensor pollicis brevis (EPB), and APL] and five intrinsic muscles [abductor pollicis brevis (APB), flexor pollicis brevis (FPB), opponens pollicis (OPP), adductor pollicis (ADP), and the first dorsal interosseus (DI_1)] actuating the human thumb [44], [46]. The first palmar interosseus is often ignored in the biomechanical analysis due to its small size, but it can theoretically aid in flexing the MCP joint of the thumb [44]. In the proposed thumb design, all the extrinsic muscle tendons were retained. For the intrinsic muscle tendons, to simplify the actuation system, the tendons that can generate similar moment potentials at the CMC joint were combined into one [60]. For example, the APB and the FPB tendons are integrated with the APL tendon into one thumb abductor tendon (ABD). And due to the minor contribution of the OPP tendon to the joint abduction, its flexion function will be the main concern so that it can be integrated with the FPL tendon. Besides, since the function of the DI_1 can be potentially performed by the ADP and the EPL, the DI_1 tendon was moved in the proposed design. Overall, the robotic thumb has five tendons, including four extrinsic muscle tendons and one ABD. The detailed tendon distribution along the thumb is shown in Fig. 2(j).

This section introduced the human finger musculoskeletal system and the bioinspired design and development of a robotic finger as well as a robotic thumb. From the bones to the tendon sheaths, in the proposed robotic finger, each component has biomimetic morphologies and structures that attempt to replicate the properties of its human finger counterpart. Likewise, it is expected that similar biomechanical advantages and the resultant human-finger-like performance can be embodied through these delicately designed and fabricated functional components. To further study the biomechanical properties and performance of the proposed robotic finger, two topics, i.e., ligamentous joint stiffness and feasible force space, are investigated through mathematical modeling and experimental verification in the following sections.

IV. Variable Joint Stiffness Associated With the Ligamentous Structure

The combined dexterity and stability of the human hand benefits a lot from the ligamentous structure of finger joints. To analyze its inner mechanism, a mathematical model of the ligamentous joint is established, and the joint stiffness is investigated in this section. It should be noted that the joint stiffness discussed here *refers in particular to the joint passive stiffness contributed by the ligaments only*. The joint active and passive stiffness acted by the muscle–tendon units is not studied in this article. Moreover, the research in [1] found that the joint capsule only contributed around 10% or less constraints in the joint displacement. Thus, the mathematical model of the ligamentous joint established here only involves the ligaments, but the experiments were conducted on the robotic finger with the integral capsuloligamentous joint so as to more closely replicate biomimetic joint properties.

A. Mathematical Model

The MCP joint is taken as an example in the analysis. Considering that the contact with the bone's convex surface may lead to a complex deformation for the ligament, the ulnar collateral ligament is chosen as the research object since it has less contact with the bone's convex surface than the radial collateral ligament. A geometrical analysis was first conducted. And a schematic diagram of the MCP joint and the associated ligament is shown in Fig. 3(a), where O is the intersection between the rotation axes of the flexion–extension motion and abduction–adduction motion, points A and B, respectively, represent the origin and insertion of the ligament, and l is the ligament's length.

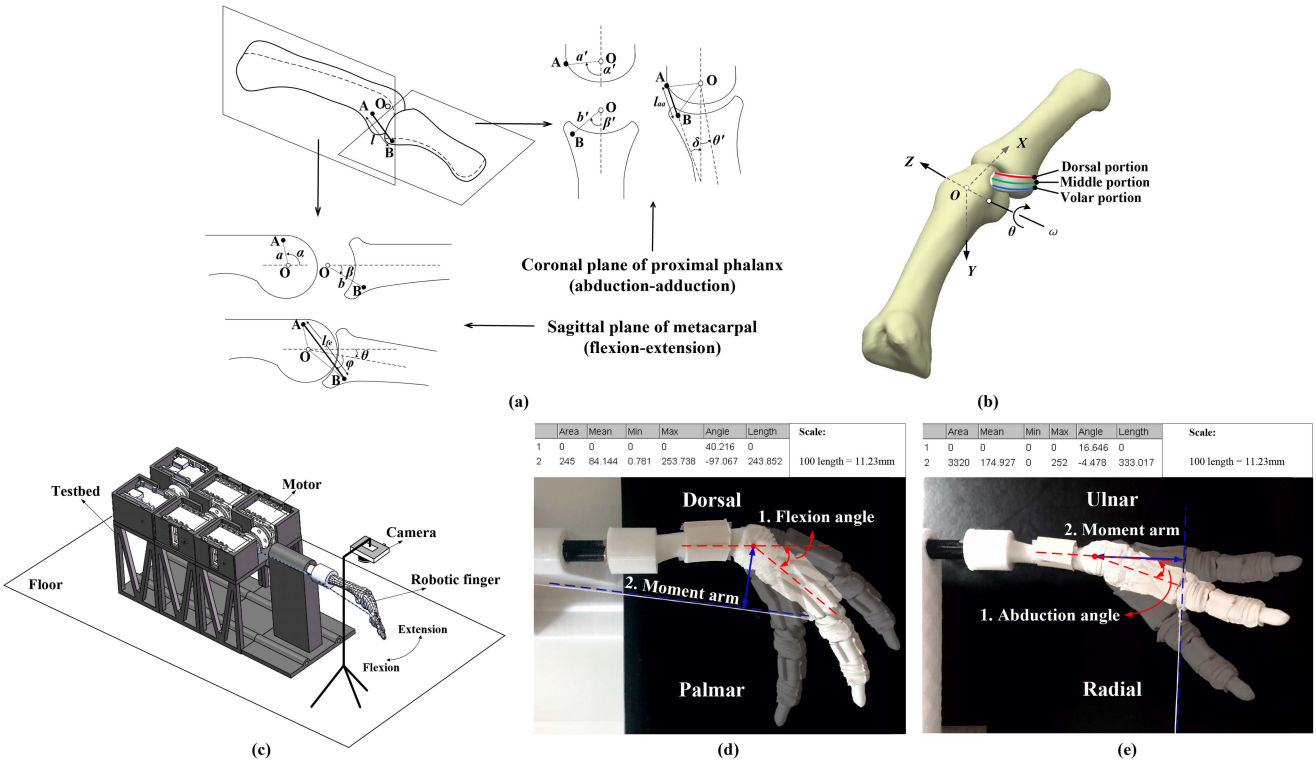

Fig. 3. Modeling and experiment about the ligamentous joint flexion and abduction stiffness. (a) Schematic diagram of the ligament's geometry in the MCP joint. (b) 3-D coordinate system in MCP joint with the ulnar ligament. (c) Experimental setup of the joint flexion stiffness test. (d) Partial view of the experimental setup of the joint flexion stiffness test. (e) Partial view of the experimental setup of the joint abduction stiffness test.

First, the joint stiffness for the flexion–extension motion was investigated. Referring to Fig. 3(a) and taking the view of the sagittal plane of the metacarpal bone (defined as the flexion–extension plane), the MCP joint is assumed to be a hinge joint during the flexion–extension motion based on the model proposed by Alexander and Bennett [61]. The metacarpal bone and proximal phalanx articulate together to form a hinge joint with the rotation axis passing through point O. As aforementioned, the ligament's origin and insertion are at points A and B, respectively. Referring to the projection in the sagittal plane, point A is at a distance a from point O along a line that makes an angle α with the long axis of the metacarpal bone, and point B is at a distance b from O along a line, forming an angle β with the long axis of the proximal bone. In this definition, the parameters a, b, α, and β are all constants that depend on the anatomical structure of the MCP joint and do not change with the motion of the joint. Besides, the bones are assumed to be rigid bodies, thus no elastic compliance or surface geometry change of the bones is considered. The distance AB, i.e., the length of the ligament observed for flexion–extension motion, is denoted as $l_{\mathrm{fe}(\theta)}$. This length varies throughout the joint flexion–extension motion. We consider an instant when the joint flexes about point O by an angle θ, relating to the angle $\angle AOB$ is $(\alpha+\beta+\theta)$ as shown in Fig. 3(a), the length $l_{\mathrm{fe}(\theta)}$ can be calculated by using the cosine law for a triangle as

$$l_{\mathrm{fe}(\theta)} = \sqrt{(a^2+b^2-2ab\cos(\alpha+\beta+\theta))}. \tag{1}$$

For simplicity, the viscous damping property of the ligament in this mathematical model is ignored. Normally, the ligament's function is performed in the elastic deformation stage. In this case, the passive tension on the ligament can be expressed as

$$F_{\mathrm{fe}(\theta)} = k\left(l_{\mathrm{fe}(\theta)} - l_e\right) + F_e. \tag{2}$$

Then, the moment arm $h_{\mathrm{fe}(\theta)}$ of the ligament to the joint in the flexion–extension plane is

$$\begin{aligned} h_{\mathrm{fe}(\theta)} &= ab\sin(\alpha+\beta+\theta)/l_{\mathrm{fe}(\theta)} \\ &= \frac{ab\sin(\alpha+\beta+\theta)}{\sqrt{(a^2+b^2-2ab\cos(\alpha+\beta+\theta))}}. \end{aligned} \tag{3}$$

Thus, the resistance torque $\tau_{\mathrm{fe}(\theta)}$ produced by the ligament in the flexion–extension direction is

$$\tau_{\mathrm{fe}(\theta)} = -F_{\mathrm{fe}(\theta)} h_{\mathrm{fe}(\theta)}. \tag{4}$$

With respect to the ligament length, the joint stiffness $K_{\mathrm{fe}(\theta)}$ for the flexion–extension can be calculated as

$$K_{\mathrm{fe}(\theta)} = \frac{\delta\tau_{\mathrm{fe}(\theta)}}{\delta\theta} = -A_{1(\theta)}\left(k - \frac{A_{2(\theta)}}{l_{\mathrm{fe}(\theta)}}\right) - \frac{A_{2(\theta)}A_{3(\theta)}}{{l_{\mathrm{fe}(\theta)}}^3}. \tag{5}$$

In (2) to (5), k is ligament elastic stiffness coefficient, l_e and F_e are the ligament's initial length and tension, respectively, when the elastic deformation (linear region) starts, $A_{1(\theta)} = ab\cos(\alpha+\beta+\theta)$, $A_{2(\theta)} = kl_e - F_e$ and $A_{3(\theta)} = a^2b^2\sin^2(\alpha+\beta+\theta)$. The result implies that the stiffness $K_{\mathrm{fe}(\theta)}$ changes with the joint flexion angle θ.

Then, the joint stiffness for the abduction–adduction motion was analyzed. The ligament's length change resulted from the flexion motion can also influence the joint stiffness in the adduction–abduction direction. Therefore, the coronal plane of the proximal phalanx (defined as the adduction–abduction plane), which is always perpendicular to the adduction–abduction rotation axis throughout the joint motion, needs to be added to elaborate the joint adduction–abduction stiffness, as shown in Fig. 3(a).

In this plane, point O represents the rotation axis of the abduction–adduction motion. The abduction–adduction rotation axis itself rotates around the flexion–extension rotation axis passing point O in the flexion–extension plane. Again, points A and B are the projection of the ligament's origin and insertion in the abduction–adduction plane. In this plane, point A is at a distance a' from point O along a line that makes an angle α' with the sagittal plane of the metacarpal bone. Point B is at a distance b' from O along a line forming an angle β' with the sagittal plane of the proximal bone. The distance between points A and B is $l_{aa(\theta')}$, representing the projection of the ligament's length in the abduction–adduction plane. In addition, the abduction–adduction rotation angle around O is defined as θ', which is approximate to zero, since only in this condition the ligament does not have too much contact with the bone convex (which will greatly complex the analysis). Thus, in the abduction–adduction plane, the angle $\angle AOB$ is $(\alpha' - \beta' + \theta')$, and similarly, the length $l_{aa(\theta')}$ can be calculated as

$$l_{aa(\theta')} = \sqrt{\left(a'^2 + b'^2 - 2a'b'\cos\left(\alpha' - \beta' + \theta'\right)\right)}. \quad (6)$$

It should be noted that the length $l_{aa(\theta')}$ is the projection of the actual ligament length in the adduction–abduction plane. To obtain the actual ligament length denoted as $l_{(\theta,\theta')}$, the angle δ between the ligament's projection in the abduction–adduction plane and the sagittal plane of the metacarpal bone, and the angle φ between the ligament's projection in the sagittal plane of the metacarpal bone and the adduction–abduction plane are required. Referring to Fig. 3(a), there exist the relations that

$$\delta = \pi - \alpha' - \arcsin\left(b'\sin\left(\alpha' + \theta' - \beta'\right)/l_{aa(\theta')}\right) \quad (7)$$

and

$$\varphi = \pi - \alpha - \theta - \arcsin\left(b\sin\left(\alpha + \beta + \theta\right)/l_{\mathrm{fe}(\theta)}\right) \quad (8)$$

where a, b, α, β, θ are the same as those defined in the flexion–extension plane. From (7) and (8), it can be seen that angle δ is related to $l_{aa(\theta')}$, and angle φ is associated with $l_{\mathrm{fe}(\theta)}$.

Consequently, length $l_{(\theta,\theta')}$ of the ligament can be implicitly represented with respect to the flexion angle θ and the adduction–abduction angle θ' as

$$\begin{aligned} l_{(\theta,\theta')} &= \sqrt{{l_{aa(\theta')}}^2\cos^2\delta/\cos^2\varphi + {l_{aa(\theta')}}^2\sin^2\delta} \\ &= l_{aa(\theta')}\sqrt{\cos^2\delta\tan^2\varphi + 1}. \end{aligned} \quad (9)$$

From (7) to (9), it can be seen that the ligament stretches with the increase of not only the flexion angle θ but also the abduction angle θ'.

Given that the ligament's property is still in the linear region, then the passive tension force $F_{l(\theta,\theta')}$ on the ligament is

$$F_{l(\theta,\theta')} = k\left(l_{(\theta,\theta')} - l_e\right) + F_e \quad (10)$$

where k is the elastic coefficient, l_e and F_e are the ligament's initial length and tension, respectively, when the elastic deformation starts.

By projecting the ligament force to the abduction–adduction plane, we can get one component F_{aa} of the ligament force that contributes to the resistance torque of the abduction–adduction motion

$$\begin{aligned} F_{aa(\theta')} &= F_{l(\theta,\theta')}\cos\eta = \left(k\left(l_{(\theta,\theta')} - l_e\right) + F_e\right)\cos\eta \\ &= kl_{aa(\theta')} - \left(kl_e - F_e\right)\cos\eta \end{aligned} \quad (11)$$

where $\eta = \arccos(l_{aa(\theta')}/l_{(\theta,\theta')}) = \arccos(1/\sqrt{\cos^2\delta\tan^2\varphi + 1})$, which is the angle between the ligament and the abduction–adduction plane.

The moment arm of the ligament force $F_{aa(\theta')}$ to the rotation axis O in the abduction–adduction plane is

$$\begin{aligned} h_{aa(\theta')} &= a'b'\sin\left(\alpha' - \beta' + \theta'\right)/l_{aa(\theta')} \\ &= \frac{a'b'\sin\left(\alpha' - \beta' + \theta'\right)}{\sqrt{\left(a'^2 + b'^2 - 2a'b'\cos\left(\alpha' - \beta' + \theta'\right)\right)}}. \end{aligned} \quad (12)$$

Thus, the resistance torque $\tau_{aa(\theta')}$ of the ligament force component $F_{aa(\theta')}$ to the joint is

$$\tau_{aa(\theta')} = -F_{aa(\theta')}h_{aa(\theta')}. \quad (13)$$

If we consider the flexion angle θ as a constant, the joint stiffness can be expressed as a function of only the abduction angle θ'. Then, the joint abduction–adduction stiffness $K_{aa(\theta')}$ affected by the change of the abduction angle θ' can be derived as (14), where

$$A_{1(\theta')} = b'\sin\left(\alpha' - \beta' + \theta'\right), A_{2(\theta')} = b'\cos\left(\alpha' - \beta' + \theta'\right)$$

$$A_{3(\theta')} = \tan\left[\alpha + \theta + \arcsin\left(A_8\right)\right]$$

$$A_{4(\theta')} = \cos\left[\alpha' + \arcsin\left(A_9\right)\right], A_{5(\theta')} = \sin\left[\alpha' + \arcsin\left(A_9\right)\right]$$

$$A_{6(\theta')} = \sqrt{a'^2 - 2a'b'\cos\left(\alpha' - \beta' + \theta'\right) + b'^2}$$

$$A_{7(\theta')} = F_e - kl_e, A_{8(\theta')} = \frac{b\sin\left(\alpha + \beta + \theta\right)}{\sqrt{a^2 - 2ab\cos\left(\alpha + \beta + \theta\right) + b^2}}$$

$$A_{9(\theta')} = \frac{b'\sin\left(\alpha' - \beta' + \theta'\right)}{\sqrt{a'^2 - 2a'b'\cos\left(\alpha' - \beta' + \theta'\right) + b'^2}}.$$

$$\begin{aligned} K_{aa(\theta')} = \frac{\delta\tau_{aa(\theta')}}{\delta\theta'} &= \frac{a'A_{7(\theta')}\left(a'{A_{1(\theta')}}^2 - A_{2(\theta')}{A_{6(\theta')}}^2\right)}{{A_{6(\theta')}}^3\sqrt{{A_{3(\theta')}}^2{A_{4(\theta')}}^2 + 1}} \\ &- \frac{a'{A_{3(\theta')}}^2A_{1(\theta')}A_{4(\theta')}A_{5(\theta')}A_{7(\theta')}\left(\dfrac{A_{2(\theta')}}{A_{6(\theta')}} - \dfrac{a'{A_{1(\theta')}}^2}{{A_{6(\theta')}}^3}\right)}{\left({A_{3(\theta')}}^2{A_{4(\theta')}}^2 + 1\right)^{\frac{3}{2}}A_{6(\theta')}\sqrt{\left(1 - {A_{1(\theta')}}^2/{A_{6(\theta')}}^2\right)}} \\ &- ka'A_{2(\theta')} \end{aligned} \quad (14)$$

It should be noted that the viscous damping property of the ligament is also ignored here for simplicity.

To further quantify and clearly describe the ligament's length and stiffness change during the joint motion, algebraic analysis is required and is presented as follows.

A Cartesian coordinate system was established at the MCP joint, as shown in Fig. 3(b). The origin bisects the tubercle of the metacarpal head. We take the distal, palmar, and radial directions as the positive X-, Y-, and Z-axis directions, respectively. The origins and insertions of the ulnar collateral ligament's dorsal, middle, and volar portions in the coordinate system are located by referring to the cadaver data from the work of Chao et al. [1].

It is evident that only the dorsal portion of the ligament has an obvious increment [1], [16], which makes it contribute most of the resistance torque and stiffness to the joint's flexion–extension motion. Considering this, the dorsal portion is taken as an example for the joint stiffness analysis.

In the coordinate system of Fig. 3(b), the ligament length can be expressed as

$$l = \sqrt{(x_i - x_o)^2 + (y_i - y_o)^2 + (z_i - z_o)^2} \tag{15}$$

where (x_i, y_i, z_i) and (x_o, y_o, z_o) are the coordinates of the ligament's insertion and origin. It should be noted that l represents the ligament length only if the ligament is in the stretched state, otherwise, l should be the distance between the ligament's origin and insertion. But it is still identified as the ligament length if there is no special emphasis needed.

We assume that the joint flexion angle is θ and the position of the origin point is constant in this MCP coordinate system. The insertion point will rotate an angle θ around the Z-axis. Thus the coordinate of the insertion point (x_{ir}, y_{ir}, z_{ir}) after the rotation can be obtained through

$$\begin{bmatrix} x_{ir} \\ y_{ir} \\ z_{ir} \end{bmatrix} = \mathbf{R}_\theta \begin{bmatrix} x_i \\ y_i \\ z_i \end{bmatrix} = \begin{bmatrix} \cos\theta & -\sin\theta & 0 \\ \sin\theta & \cos\theta & 0 \\ 0 & 0 & 1 \end{bmatrix} \begin{bmatrix} x_i \\ y_i \\ z_i \end{bmatrix} \tag{16}$$

where $\mathbf{R}_\theta$ is the rotation matrix. Then the ligament length change during the whole joint flexion motion can be calculated.

Since the flexion–extension motion is in the X–Y plane, the moment arm of the ligament to the joint is the distance from the projection of the rotation axis to the projection of the ligament in the X–Y plane. In this plane, the rotation axis is projected to a point $(0, 0)$, and the ligament is projected to a line through the point (x_o, y_o) and (x_i, y_i). Then, the linear equation of the ligament's projection can be expressed as

$$\frac{y_i - y_0}{x_i - x_0} x - y + y_0 - \frac{y_i - y_0}{x_i - x_0} x_0 = 0. \tag{17}$$

Thus, the moment arm M of the ligament to the joint $(0, 0)$ in flexion–extension motion can be obtained

$$M = \frac{\left| y_0 - \dfrac{y_i - y_0}{x_i - x_0} x_0 \right|}{\sqrt{\left(\dfrac{y_i - y_0}{x_i - x_0} \right)^2 + 1}}. \tag{18}$$

Assuming that the ligament's deformation is in the linear region, thus the passive tension F on the ligament can be expressed as

$$F = F_0 + k\Delta l_0 \tag{19}$$

where k is the elastic coefficient, F_0 is the initial tension of the linear region, Δl_0 is the ligament's length change in the linear region, and (x_e, y_e, z_e) is the location of the ligament's insertion when the ligament starts the elastic deformation. Thus, it has

$$\begin{cases} \Delta l_0 & = l_{io} - l_{eo} \\ l_{io} & = \sqrt{(x_i - x_o)^2 + (y_i - y_o)^2 + (z_i - z_o)^2} \\ l_{eo} & = \sqrt{(x_e - x_o)^2 + (y_e - y_o)^2 + (z_e - z_o)^2}. \end{cases}$$

However, if we consider the whole realistic process of the ligament deformation, the initial state of the ligament could be slack. Then according to its load-deformation property, the passive tension F on the ligament should go through three phases, i.e., no tension when the distance between the ligament's origin and insertion is shorter than its original length; in the toe region at the initial deformation stage; and in the elastic region when the length of the ligament keeps increasing. Thus, three functions are adopted here to piecewise fit the entire changing process of the passive tension F, which are

$$\begin{cases} F = 0 & l_d - l_i \leqslant 0 \\ F = \dfrac{F_0}{l_0}(l_d - l_i) & 0 < l_d - l_i < l_0 \\ F = f(l_d - l_i) & l_d - l_i \geqslant l_0 \end{cases} \tag{20}$$

where l_d is the distance between the ligament's origin and insertion which can be directly calculated by (15), l_i is the ligament's original length, l_0 and F_0 are the length and the passive tension of the ligament at the end of the toe region, and $f(x)$ in the third equation of (20) is the fitting function of the ligament's load-deformation relation in the elastic region.

For the robotic finger proposed in this research, the coordinates of the ligament's origin and insertion are $(2.5, -3.5, -4.51)$ and $(10.5, -3, -5.22)$, respectively. The ligament's original length l_i is given as 12.56 mm, and the corresponding l_0 and F_0 for the artificial ligament are 0.1525 mm and 0.075 N. These parameters were identified by referring to the cadaveric data from Chao et al. [1], but with minor modifications according to the adopted fabrication method and materials. For instance, the locations of the ligament's origin and insertion were slightly modified from the cadaveric data for easy assembly and good structural reliability. Besides, the function $f(x)$ is defined by using a three-order polynomial to fit the experiment data from the artificial ligament load-deformation test, and it has

$$f(x) = -7.853x^3 + 44.55x^2 + 0.1908x - 0.962. \tag{21}$$

The resistance torque τ in the flexion–extension motion is generated by the component of the ligament's tension force in the flexion–extension plane, it has

$$\tau = -F \cos\gamma M \tag{22}$$

where $\gamma = \arcsin(|\boldsymbol{n}_l \boldsymbol{n}_{\mathrm{fe}}|/(|\boldsymbol{n}_l||\boldsymbol{n}_{\mathrm{fe}}|))$, which is the angle between the ligament and the flexion–extension plane. In

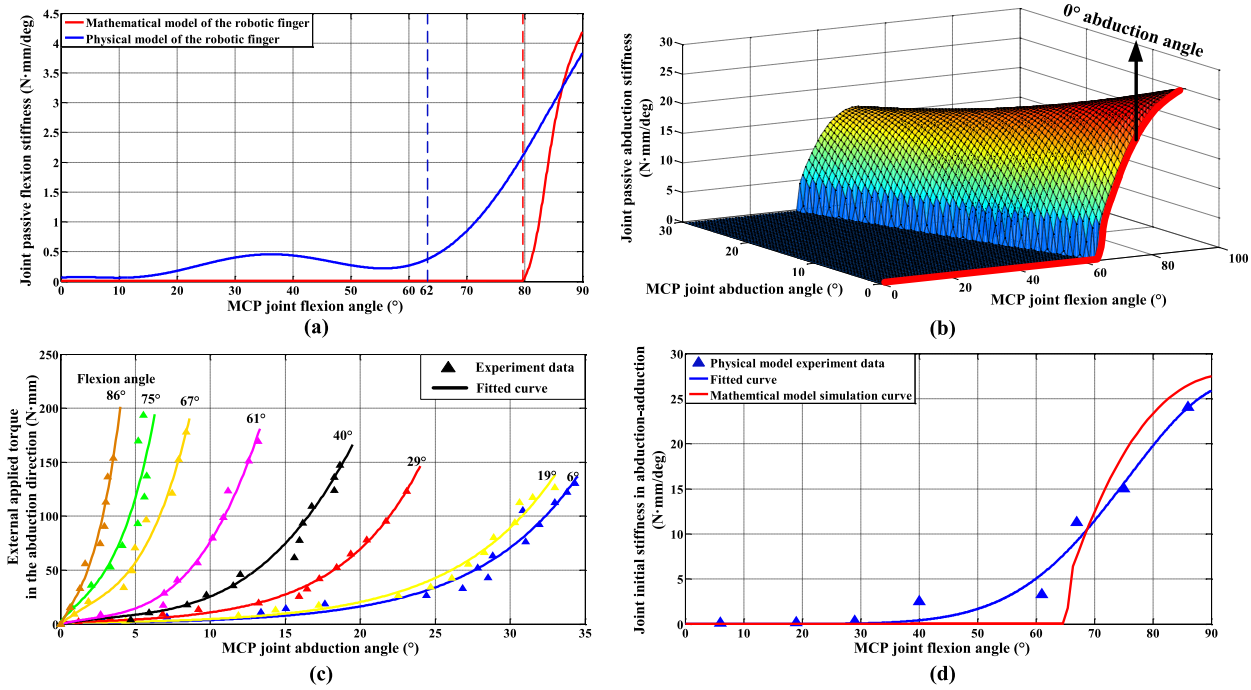

Fig. 4. Theoretical and experiment results of the joint flexion and abduction stiffness. (a) Comparison results of the joint passive flexion stiffness (blue-physical model experiment, red-mathematical model simulation). (b) Joint passive abduction stiffness of the mathematical model simulation (with the red line indicating the joint abduction stiffness at 0° abduction angle). (c) Joint external applied torque of the physical model changing with the abduction angles at various flexion angle positions. (d) Comparison results of the joint abduction stiffness at 0° abduction angle (blue-physical model experiment, red-mathematical model simulation).

the expression of γ, $\boldsymbol{n}_l$ is the vector of the ligament and $\boldsymbol{n}_{\text{fe}}$ is the unit normal vector of the flexion–extension plane. Thus, it can be calculated and expressed as $\gamma = \arcsin(|z_i - z_o|/\sqrt{(x_i - x_o)^2 + (y_i - y_o)^2 + (z_i - z_o)^2})$.

The negative sign in (22) means the torque impedes the flexion motion. Then, the joint stiffness contributed by the dorsal portion of the ulnar ligament can be obtained with the function

$$K_{\text{fe}} = \frac{\delta\tau}{\delta\theta}. \tag{23}$$

With the derivations above, the theoretical relationship of the passive joint stiffness to the flexion angle is obtained, which is shown as the red line in Fig. 4(a). The flexion angle θ reaches around 80°, where the discontinuity of stiffness change at about 80° may be caused by the piecewise fitting function of the passive tension F in (20).

In addition, stiffness variation in the adduction–abduction direction is investigated as follows.

An instantaneous rotation axis of the adduction–abduction motion needs to be established in the MCP joint coordinate system. At the beginning of the flexion, this instantaneous rotation axis coincides with the Y-axis, followed by a continuous rotation around the Z-axis during the flexion motion. Taking the ulnar ligament as the study object, the analysis is focused on the abduction motion where the direction vector $\mathbf{r}_0$ of the initial rotation axis is along the negative Y-axis [expressed with the vector $(0, -1, 0)$ in Fig. 3(b)].

Likewise, based on the coordinate system established in Fig. 3(b), the ligament length (the distance between the ligament's origin and insertion) can be expressed as

$$l' = \sqrt{(x'_i - x'_o)^2 + (y'_i - y'_o)^2 + (z'_i - z'_o)^2} \tag{24}$$

where $(x_i,' y_i,' z_i')$ and $(x_o,' y_o,' z_o')$ are the coordinates of the ligament's insertion and origin. To obtain the ligament length, the positions of the insertion during the whole abduction motion are needed.

In the condition that the joint's flexion angle is θ, the abduction rotation axis $\boldsymbol{r}$ should be

$$\begin{aligned}\boldsymbol{r} &= \mathbf{R}_z(\theta)\,\boldsymbol{r}_0 \\ &= \begin{bmatrix}\cos\theta & -\sin\theta & 0\\ \sin\theta & \cos\theta & 0\\ 0 & 0 & 1\end{bmatrix}\begin{bmatrix}0\\-1\\0\end{bmatrix} = \begin{bmatrix}\sin\theta\\-\cos\theta\\0\end{bmatrix}\end{aligned} \tag{25}$$

where $\mathbf{R}_z(\theta)$ is the rotation matrix, and $\boldsymbol{r}_0$ is the initial abduction rotation axis.

Assuming that the abduction angle is θ', the position of the insertion after the flexion and abduction motion can be expressed as

$$\begin{bmatrix}x_{i'fa}\\ y_{i'fa}\\ z_{i'fa}\end{bmatrix} = \mathbf{R}_r(\theta')\begin{bmatrix}x_{i'}\\ y_{i'}\\ z_{i'}\end{bmatrix}. \tag{26}$$

In (26), $\mathbf{R}_r$ is the Rodrigues rotation matrix having the form

$$\mathbf{R}_r = \mathbf{I} + (1 - \cos(\theta'))\,\mathbf{K}^2 + \sin(\theta')\,\mathbf{K} \tag{27}$$

in which $\mathbf{I}$ is the standard identity matrix and $\mathbf{K}$ is the cross product matrix of the abduction rotation axis $\boldsymbol{r}$. Therefore, the distance between the ligament's origin and insertion during the whole abduction motion can be calculated.

The moment arm of the ligament to the joint in the abduction–adduction motion is in the coronal plane of the proximal phalanx. And this coronal plane rotates an angle of θ around the Z-axis in the MCP joint coordinate system. Since a plane in a 3-D coordinate system can be expressed as $Ax + By + Cz + D = 0$, we have the abduction–adduction plane as

$$x \tan\theta - y = 0. \tag{28}$$

In this plane, the projection of the rotation axis is still the point $(0, 0, 0)$. The ligament's origin $(x_o,' y_o,' z_o')$ and insertion $(x_i,' y_i,' z_i')$ are projected to the point $(x_{op},' y_{op},' z_{op}')$ and $(x_{ip},' y_{ip},' z_{ip}')$. According to point-to-surface projection formula in space, we have

$$\begin{cases} x'_{op} = (x'_o + y'_o \tan\theta)/(\tan^2\theta + 1) \\ y'_{op} = (y'_o \tan^2\theta + x'_o \tan\theta)/(\tan^2\theta + 1) \\ z'_{op} = z'_o. \end{cases} \tag{29}$$

The same with the projection of the point $(x_{ip},' y_{ip},' z_{ip}')$. Then, the moment arm M' should be the distance from the point $(0, 0, 0)$ to the line L, which is through the point $(x_{op},' y_{op},' z_{op}')$ and $(x_{ip},' y_{ip},' z_{ip}')$. The line L can be expressed in a two-point form

$$\frac{x - x'_{op}}{x'_{ip} - x'_{op}} = \frac{y - y'_{op}}{y'_{ip} - y'_{op}} = \frac{z - z'_{op}}{z'_{ip} - z'_{op}}. \tag{30}$$

Then, the vertical coordinate (x_v, y_v, z_v) from point $(0, 0, 0)$ to the line L can be obtained

$$\begin{cases} x_v = (x'_{ip} - x'_{op})\, t + x'_{op} \\ y_v = \left(y'_{ip} - y'_{op}\right) t + y'_{op} \\ z_v = (z'_{ip} - z'_{op})\, t + z'_{op} \end{cases} \tag{31}$$

where

$$t = \frac{(x'_{op} - x'_{ip})\, x'_{op} + \left(y'_{op} - y'_{ip}\right) y'_{op} + (z'_{op} - z'_{ip})\, z'_{op}}{(x'_{ip} - x'_{op})^2 + \left(y'_{ip} - y'_{op}\right)^2 + (z'_{ip} - z'_{op})^2}.$$

Thus, the moment arm M' should be the distance from the point $(0, 0, 0)$ to the point (x_v, y_v, z_v), which is shown in

$$M' = \sqrt{{x_v}^2 + {y_v}^2 + {z_v}^2}. \tag{32}$$

Likewise, the passive tension F' on the ligament can be expressed as

$$F' = F_0 + k\Delta l_0 \tag{33}$$

where k is the elastic coefficient, F_0 is the initial tension of the linear region, Δl_0 is the ligament's length change in the linear region, and $(x_e,' y_e,' z_e')$ is the location of the ligament's insertion when the ligament starts the elastic deformation. Thus, it has

$$\begin{cases} \Delta l_0 = l'_{io} - l'_{eo} \\ l'_{io} = \sqrt{(x'_i - x'_o)^2 + (y'_i - y'_o)^2 + (z'_i - z'_o)^2} \\ l'_{eo} = \sqrt{(x'_e - x'_o)^2 + (y'_e - y'_o)^2 + (z'_e - z'_o)^2}. \end{cases}$$

In this case, from the view of the actual situation, the passive tension F' also needs to be formulated as the piecewise function in (20).

Since the resistance torque τ' in the abduction–adduction motion is generated by the component of the ligament's tension force in the abduction–adduction plane, it has

$$\tau' = -F' \cos\eta M'. \tag{34}$$

The negative sign in (34) means the torque impedes the abduction motion. And η in (34) is the angle between the ligament and the abduction–adduction plane, it yields

$$\cos\eta = \frac{A_1 + A_2 + A_3}{A_4 A_5} \tag{35}$$

where

$$A_1 = (x'_i - x'_o)\,(x'_{ip} - x'_{op}),\ A_2 = (y'_i - y'_o)\left(y'_{ip} - y'_{op}\right)$$

$$A_3 = (z'_i - z'_o)\,(z'_{ip} - z'_{op})$$

$$A_4 = \sqrt{(x'_i - x'_o)^2 + (y'_i - y'_o)^2 + (z'_i - z'_o)^2}$$

$$A_5 = \sqrt{(x'_{ip} - x'_{op})^2 + \left(y'_{ip} - y'_{op}\right)^2 + (z'_{ip} - z'_{op})^2}.$$

Then, the joint stiffness contributed by the dorsal portion of the ulnar ligament can be obtained with a function as

$$K_{aa} = \frac{\delta\tau'}{\delta\theta'}. \tag{36}$$

The joint abduction stiffness changed with the flexion and abduction angles is shown in Fig. 4(b). With respect to each abduction angle in the range of $[0^\circ, 30^\circ]$, the joint abduction stiffness all goes through a sudden ascent from zero when gradually increasing the flexion angles. It should be noted that the abduction motion of the joint will bend the ligament due to the contact between the ligament and the articular surface, leading to an additional increment of the ligament's length. Thus the joint abduction stiffness in small abduction angles should be mainly considered in this result. For instance, the joint passive abduction stiffness variation process at 0° abduction angle is marked out by a red line on the edge of the curved surface in Fig. 4(b). This edge line is also adopted to compare with the physical model experiment result as the red curve in Fig. 4(d). As can be seen at 0° abduction angle, the joint abduction stiffness maintains at zero before the flexion angle reaches around 65°, meaning that the ligament keeps slack or in the toe region during this process. After that, the joint stiffness steeply climbs and reaches the maximum value at 90° flexion angle (full flexion position). Likewise, the discontinuity of the red theoretical curve also results from the piecewise function of the ligament tension F'.

The above presents the theoretical analysis of the joint stiffness that is determined by the deformation of the associated

ligamentous structure. Apart from the individual variation of the joint stiffness in both flexion–extension and abduction–adduction directions, we can also see from Fig. 4(a) and (d) that the joint stiffness varies differently in the two directions, indicating the anisotropic property of the joint stiffness. One of the differences is the position of the discontinuity on the curve, of which the discontinuity point of the joint stiffness in the flexion–extension direction appears at around 80° flexion angle but that in the abduction–adduction direction is at about 65° flexion angle. The larger range of the low joint stiffness in the flexion–extension direction is expected to benefit more the joint's dexterity. Another difference is presented on the magnitude of the joint stiffness. It can be seen from Fig. 4(a) and (d) that the maximum value of the joint stiffness in the flexion–extension direction is about 4 N · mm/deg (at 90° flexion angle), which is much smaller compared with about 27 N · mm/deg maximal joint stiffness (at 90° flexion angle) in the abduction–adduction direction. The greater joint stiffness in the abduction–adduction direction contributes to maintaining the grasping stability, especially when subject to perturbation forces from the lateral sides. To verify these results, experiments are then conducted in the following section.

B. Experimental Verification

To verify the results from the mathematical analysis, the flexion and abduction stiffness for the MCP joint in the robotic finger were tested based on the prototype developed in this article. Fig. 3(c) shows the experimental setup for testing the joint flexion stiffness, where a robotic finger proposed in Section III was placed on a testbed. The proximal end of the metacarpal was fixed on the testbed, and a motor was connected to the distal end of the proximal phalanx through a string and a pulley. In the setup, the flexion–extension plane was in the horizontal direction parallel to the floor, and so was the string that was connected to the motor. Such an arrangement helps remove the influence of gravity. During the experiment, at each step, the motor pulled the string to flex the MCP joint by a small angle. The tension force on the string was obtained from the feedback torque of the motor, the flexion angle and the moment arm (which was the shortest distance from the rotation axis to the string) were captured by a camera, shown in Fig. 3(d). The motion of each step was recorded by the camera, and the images (including the angle numbered by 1 and distance numbered by 2) were then processed and analyzed in the software ImageJ. Fig. 3(d) only shows three positions of the robotic finger during flexion, and the one in the second position was selected to show the measurement. Here, according to the size of the image, the measurement scale of the length was identified as 100 length $= 11.23$ mm. In data processing, the externally applied torque T was calculated as $T = FL$, where F is the tension force on the string, and L is the moment arm. Note that, in this case, the external applied torque is equivalent to the MCP joint's internal resistance torque. Using the relation that $K = d\tau/d\theta$, joint stiffness in the flexion–extension direction from the experiment can be calculated. Referring to Fig. 4(a), the blue line shows the physical experiment results, and the red line implies the theoretical results. Both results show that the joint flexion stiffness maintains at a low value in most of the flexion positions but then rapidly increases near the full flexion position.

Subsequently, the MCP joint abduction stiffness was also tested against various abduction angles, and the tests were conducted at a series of flexion positions. The partial view of the experimental setup is shown in Fig. 3(e). In this case, the abduction–adduction plane (frontal plane) in this setup is always perpendicular to the floor. There are two motors controlling the MCP joint flexion and abduction angles, respectively. The string for the flexion motion (motor 1) was connected to the distal end of the proximal phalanx on the palmar side with its direction parallel to the floor. The motor for abduction motion (motor 2) was located below the finger with its string vertical to the floor, connected to the distal end of the proximal phalanx on the radial side. In the test, the MCP joint was driven to flex at a specified angle, and at each flexion position, motor 2 drove the joint to deform gradually in the abduction–adduction direction. During this process, the abduction angles, the tension force on the string, and the moment arm were recorded so as to obtain the passive joint abduction stiffness. The measurement and calculation methods are the same as those used in the joint flexion stiffness test.

Through the above experiment, the relation of the joint torques and the joint abduction angles in different flexion angle conditions could be obtained and was illustrated as a group of curves in Fig. 4(c). As can be seen, the larger the flexion angle, the more rapidly the joint torques increase with the abduction angle increasing, implying the higher abduction joint stiffness. Furthermore, similar to the mathematical analysis, the joint abduction stiffness at 0° abduction angle is taken as the evaluation index. It can be identified as the slope of the tangent line of each torque–angle curve at the origin point, as shown in Fig. 4(c). These 0° joint abduction stiffness values at all the preselected flexion angles are marked as the blue triangles in Fig. 4(d). The blue curve is fitted with respect to the points denoted with triangles to describe the change of the 0° joint abduction stiffness with respect to the flexion angle. In Fig. 4(d), both of the results from the experiment and mathematical analysis present a similar rising trend of the 0° joint abduction stiffness when the flexion angle increases. For the experimental result, the joint abduction stiffness starts to rapidly grow at around 55° flexion angle, showing good similarity with the mathematical result where the surging point appears at about 65° flexion angle. The results show good consistency with those of the cadaver test in [1]. Besides, these results evidence that the ligamentous joint stiffness properties are anisotropic. Specifically, the joint stiffness in the flexion–extension direction keeps at low values in a larger flexion angle range $[0^\circ, 62^\circ]$ compared with that in the abduction–adduction direction $[0^\circ, 55^\circ]$. Moreover, the joint stiffness in the abduction–adduction direction is of higher magnitude than in the flexion–extension direction. In other words, though the joint stiffness properties in these two directions are coupled through the same collateral ligaments' deformation, their behaviors are not identical. Therefore, if we combine these two groups of joint stiffness values into one matrix, this stiffness matrix will be nondiagonal.

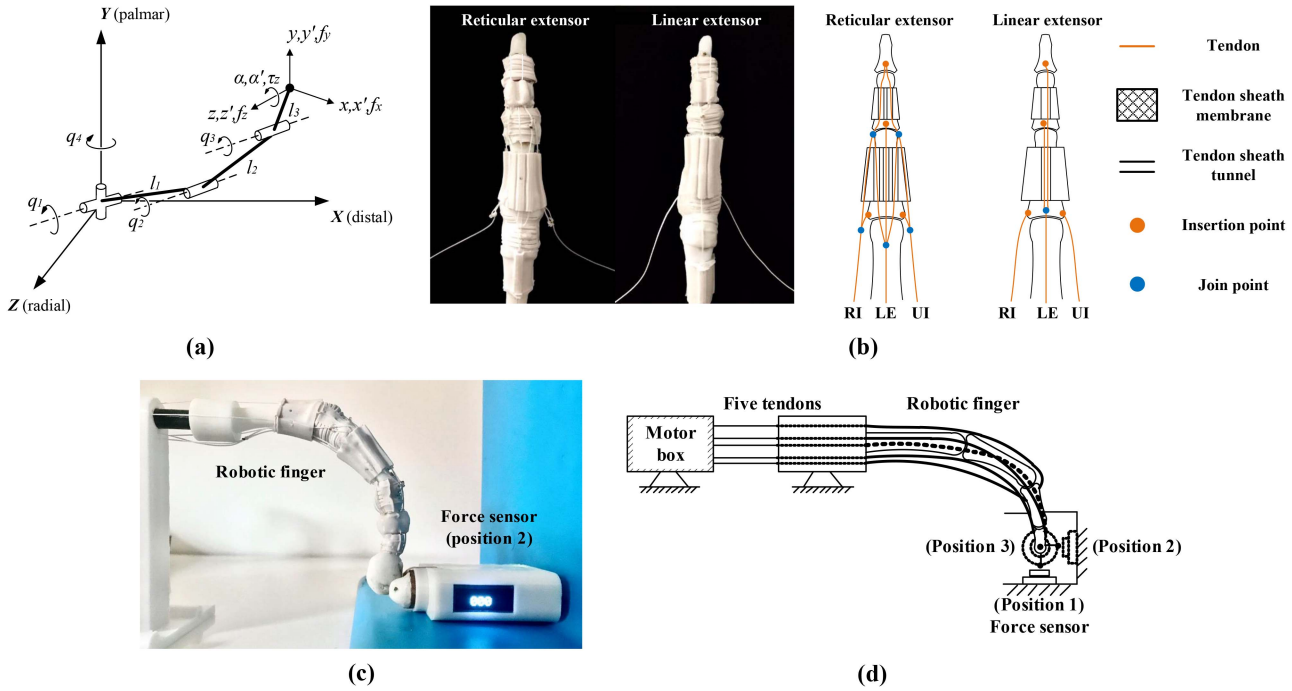

Fig. 5. Modeling and experiment about the effect of extensor mechanism on fingertip feasible force space. (a) Kinematic model of the robotic index finger. (b) Physical models and the schematic diagrams of the robotic fingers with reticular and linear extensor (dorsal view). (c) Physical model of the fingertip force testbed. (d) Schematic diagram of the fingertip force testbed.

From the above investigation, it can be seen that the stiffness in the MCP joint is not constant but varies with joint angles. This anisotropic variable stiffness behavior exists in both flexion–extension and abduction–adduction directions, which provides the fundamental biomechanical conditions for the versatile, adaptive, dexterous, and stable performance of human and robotic fingers. Especially, in the abduction–adduction direction, the performance of low stiffness in a small flexion angle maintains good joint dexterity, and the high stiffness near the full flexion position provides the joint with good lateral force bearing capability. This unique joint property is directly generated from interaction postures and simultaneously acts on the interaction process, such as pulling a rope with a tight grip posture.

V. Enlarged Feasible Force Space Associated With the Extensor Mechanism

It was found that the extensor mechanism exerts a significant influence on the fingertip's feasible force space. This section aims to evidence this statement through both mathematical modeling and experimental study.

A. Mathematical Calculation and Numerical Simulation of the Feasible Force Space

According to the research of Valero-Cuevas [3], the kinematic model of an index finger with four rotational degrees of freedom (DOFs) is established in Fig. 5(a). In this analysis, without loss of generality, the DIP and PIP joints are considered as revolute joints, and the MCP joint is treated as a 2-DOF universal joint.

To obtain the feasible force space at the fingertip, a mapping from the muscular actions to the joints and then to the fingertip's mechanical outputs needs to be identified. To formulate the mapping, an inertial reference coordinate system O-XYZ is established with the origin located at the geometrical center of the metacarpal bone's head. In addition, a local coordinate frame is attached at the fingertip. In the model [see Fig. 5(a)], the lengths of the three links are l_1, l_2, and l_3, respectively. The joint angles are organized as a vector $\mathbf{q} = (q_1, q_2, q_3, q_4)$ and the fingertip posture is represented by a vector $\mathbf{p} = (x, y, z, \alpha)$. The rotational kinetic inputs are the four net joint torques $(\tau_1, \tau_2, \tau_3, \tau_4)$ that produce the fingertip output forces/torque as (f_x, f_y, f_z, τ_z).

According to the mathematical model in Fig. 5(a), the forward kinematics model was derived in (37) and its Jacobian matrix can be correspondingly obtained with s_1 meaning $\sin q_1$, c_1 standing for $\cos q_1$ and c_{123} representing $\cos(q_1 + q_2 + q_3)$

$$\begin{pmatrix} x \\ y \\ z \\ \alpha \end{pmatrix} = \begin{pmatrix} (l_1 c_1 + l_2 c_{12} + l_3 c_{123})\, c_4 \\ l_1 s_1 + l_2 s_{12} + l_3 s_{123} \\ (l_1 c_1 + l_2 c_{12} + l_3 c_{123})\, s_4 \\ q_1 + q_2 + q_3 \end{pmatrix}. \tag{37}$$

Using the kinematics and based on the principle of virtual work, we can map the joint torques $\boldsymbol{\tau}$ to the static fingertip wrench $\boldsymbol{w}$ as

$$\boldsymbol{w} = \mathbf{J}(\boldsymbol{q})^{-T} \boldsymbol{\tau} \tag{38}$$

where $\boldsymbol{\tau} = (\tau_1, \tau_2, \tau_3, \tau_4)$, $\boldsymbol{w} = (f_x, f_y, f_z, \tau_z)$, and $\mathbf{J}(\boldsymbol{q})$ is the Jacobian matrix.

In the proposed robotic finger, five motors are used to drive the four rotational DOFs. The five tendon forces f can be obtained by multiplying the tendon maximum forces diagonal matrix $\boldsymbol{F} \in \mathbb{R}^{5\times5}$ with the activation levels $\boldsymbol{a} = (a_1, a_2, a_3, a_4, a_5)$,

where the subscripts 1, 2, 3, 4, and 5, respectively, correspond to the RI, UI, FDP, LE, and FDS muscles, and $0 \leq a_i \leq 1$, for $i = 1, 2, 3, 4$ and 5. Based on these [3], the joint torques can alternatively be derived from the actuation forces and the moment arms as (39). Equation (39) presents the mapping from the tendon forces to the joint torques, where $\mathbf{R}(\boldsymbol{q}) \in \mathbb{R}^{4\times5}$ is a moment arms matrix, with 4 rows meaning four DOFs and 5 columns meaning five muscle tendons. Each entry of $\mathbf{R}(\boldsymbol{q})$ is a signed scalar moment arm value $r(\boldsymbol{q})_{i,j}$ that transforms the positive tendon force into the torques at the corresponding joints, where *i* indicates the DOF (1–4), and *j* indicates the muscle tendon (1–5). Combining (38) and (39), the mapping from the input muscle force space to the fingertip output wrench space can be expressed as (40). In (40), $\boldsymbol{w} = (\boldsymbol{w}_1, \boldsymbol{w}_2, \boldsymbol{w}_3, \boldsymbol{w}_4, \boldsymbol{w}_5)^T$, where the 4×1 column vectors $\boldsymbol{w}_i$ calculated from matrix $\mathbf{J}(\boldsymbol{q})^{-T}\mathbf{R}(\boldsymbol{q})\boldsymbol{F}$ are the generators of the Minkowski sum [62]

$$\boldsymbol{\tau} = \mathbf{R}(\boldsymbol{q})\boldsymbol{f} = \mathbf{R}(\boldsymbol{q})\boldsymbol{F}\boldsymbol{a} \tag{39}$$

$$\boldsymbol{w} = \mathbf{J}(\boldsymbol{q})^{-T}\mathbf{R}(\boldsymbol{q})\boldsymbol{F}\boldsymbol{a}. \tag{40}$$

Therefore, all the possible forces that the motor–tendon system is able to produce at the fingertip in a particular posture can be described in a zonotope called the feasible wrench set. If we assume the output torque τ_z as zero, all the output will be forces, and thus the feasible wrench set can be regarded as the feasible force set of the fingertip. In addition, in (40), $\mathbf{J}(\boldsymbol{q})^{-T}$ can be calculated from the geometry and the posture of the finger, and $\mathbf{R}(\boldsymbol{q})$ can be obtained through the experiment for testing the relationship between each joint angle change δq and each tendon excursion δs. Besides, $\boldsymbol{F}$ refers to the maximum force, which is derived from the maximum torque that the motors can generate.

As an example, a standard finger posture (with DIP at 10°, PIP at 45°, MCP flexion at 45°, and abduction at 0°) is selected to find the feasible force set [25], [63]. Herein, the structure parameters for the Jacobian matrix of the robotic finger with the reticular extensor are specified as $l_1 = 0.0455$ m, $l_2 = 0.0258$ m, $l_3 = 0.0169$ m, $q_1 = \pi/4$, $q_2 = \pi/4$, $q_3 = \pi/18$ and $q_4 = 0$, and $\mathbf{J}(\boldsymbol{q})^{-T}$ can be obtained as (41) in Appendix A.

Furthermore, in order to accurately define the moment arm matrix $\mathbf{R}(\boldsymbol{q})$, we tested the relationship between the tendon excursion and the joint angle, with the results being consistent with the cadaveric test results in Chao et al. [1]. Thus, the moment arm of each tendon to the finger joint was obtained, with the minus sign standing for the cases that the muscles contribute negative torques to the joint angle increase. The detailed moment arm matrix formulation is provided in (43) in Appendix B. It is noted that the slack phenomena of the tendons should be avoided to accurately obtain the relationship between the tendon excursion and the joint angle. When the finger is in a full extension position, there is a pretension force on each tendon, which is generated by manually rotating the motors to pull the tendons until all the tendons are straightened. Consequently, considering the maximum torque of the actual motors in the physical prototype, we set the maximum tendon force as 9 N. Thus, the generators $\boldsymbol{w}_i$ of the fingertip output force can be calculated (the detailed calculation process of getting the generators is provided in Appendix C). The resultant feasible force set at the standard posture is illustrated in Fig. 6(a). Furthermore, based on the five force vectors in the feasible force set, the feasible force space can be calculated and plotted using minksum and convhull functions embedded in Matlab, as shown in Fig. 6(b).

TABLE I
VOLUME OF THE FEASIBLE FORCE SPACE OF DIFFERENT MODELS

Model		Posture		
		Posture 1	Posture 2	Posture 3
Mathematical	Reticular extensor	88.9320	65.4249	78.4928
	Linear extensor	72.3628	44.4784	63.9485
	Improvement	22.9 %	47.1 %	22.7 %
Physical	Reticular extensor	39.8599	17.3209	34.4450
	Linear extensor	19.8477	9.5869	9.6287
	Improvement	100.8 %	80.7 %	257.7 %

To compare the theoretical influences on the feasible force space from the reticular and linear extensors, the geometry, moment arm, and tendon force parameters of the two robotic fingers with different extensors were substituted into the mathematical model. All the parameters of the two robotic fingers are the same except the moment arm matrixes which were obtained from the tendon excursion-joint angle test on each finger prototype. Thus, the moment arm matrixes of the two robotic fingers in three postures (posture 1 (open posture) is given as DIP at 5°, PIP at 15°, MCP flexion at 40°, and abduction at 0°, posture 2 (close posture) as DIP at 15°, PIP at 60°, MCP flexion at 80°, and abduction at 0°, and posture 3 (standard posture) as DIP at 10°, PIP at 45°, MCP flexion at 45°, and abduction at 0°) were calculated and provided from (43) to (48) in Appendix B. The comparison results of the feasible force space are shown in Fig. 6(d), (e), and (f). It can be seen that larger feasible force space is obtained by the robotic finger with a reticular extensor (the yellow block) compared with that with a linear extensor (the green block). To make a more intuitive comparison, the mathematical results of the corresponding feasible force space volume are presented in Table I. Compared with using the linear extensor, the feasible force space volume of the robotic finger can improve 22.9% in posture 1, 47.1% in posture 2, and 22.7 % in posture 3 when using the reticular extensor, showing an average of 30.9% enlargement. Additionally, to compare with the human finger, the mathematical model with the human finger cadaveric data [2], [64] in standard posture (posture 3) was also analyzed with the result shown as the purple block in Fig. 6(c). The transpose of the inverse of the Jacobian matrix, the moment arm matrix, and the calculated fingertip force generators of the human index finger are, respectively, provided in Appendix A [see (42)], E [see (49)], and F [see (52)]. Noting that the tendon force inputs of both the human and robotic fingers are set as the same (9 N for each tendon), it can be seen that the feasible force space of the robotic finger is apparently larger than that of the human finger. The reason could be the innate differences in the joint moment arms and the phalangeal dimensions.

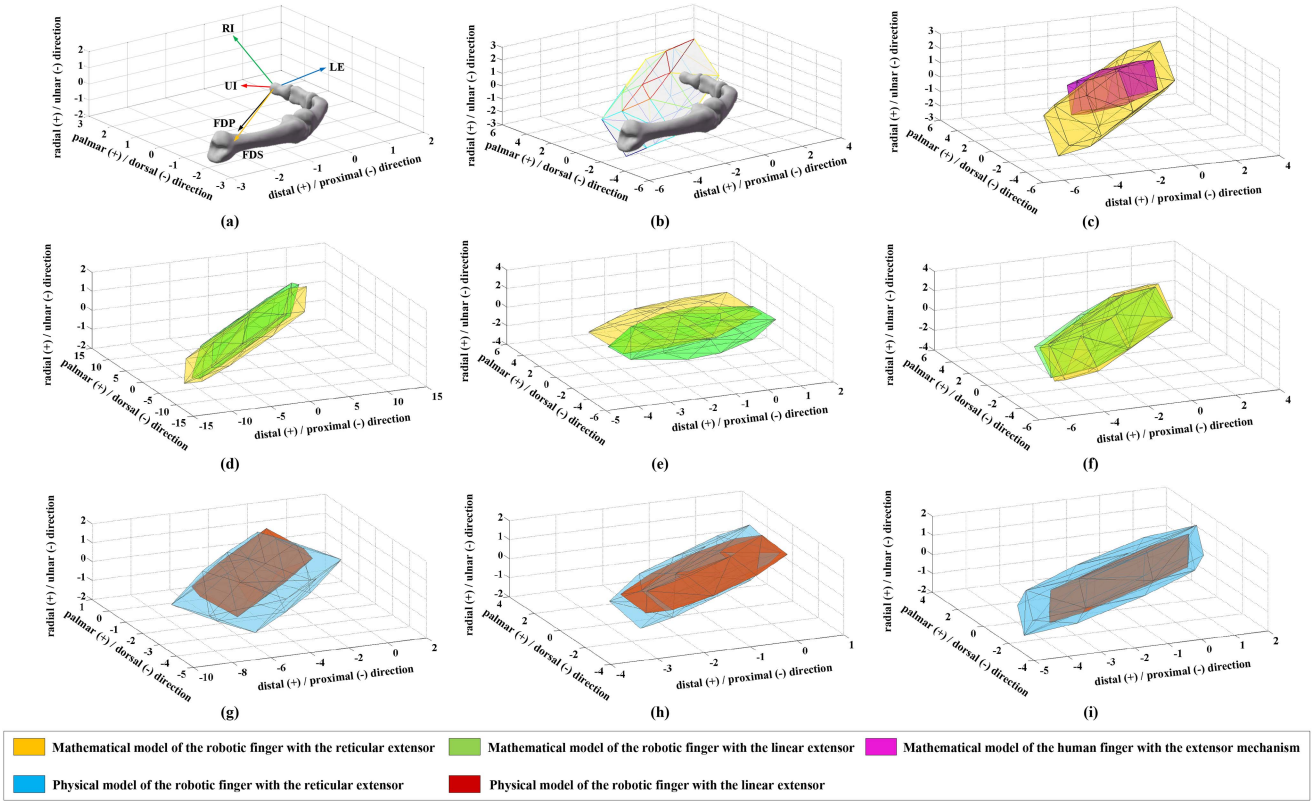

Fig. 6. Theoretical and experiment results of the feasible force space with different extensor structures. (a) Feasible force set calculated from robotic finger's mathematical model. (b) Feasible force space generated from the feasible force set of the robotic finger's mathematical model. (c) Theoretical comparison results of the human and robotic fingers in posture 3. (d) Theoretical comparison results of different robotic fingers in posture 1. (e) Theoretical comparison results of different robotic fingers in posture 2. (f) Theoretical comparison results of different robotic fingers in posture 3. (g) Experimental comparison results of different robotic fingers in posture 1. (h) Experimental comparison results of different robotic fingers in posture 2. (i) Experimental comparison results of different robotic fingers in posture 3 (Note: Yellow-mathematical model of the robotic finger with the reticular extensor; green-mathematical model of the robotic finger with the linear extensor; purple-mathematical model of the human finger with the extensor mechanism; blue-physical model of the robotic finger with the reticular extensor; red-physical model of the robotic finger with the linear extensor).

B. Experimental Verification

To investigate and verify the effect of the network structure of the extensor mechanism on the feasible force space, two physical prototypes of robotic fingers were designed and fabricated, one with a reticular extensor (mimicking the extensor mechanism in human fingers) and the other with a linear extensor, as shown in Fig. 5(b). To better illustrate the different morphologies of the reticular and linear extensor, the schematic diagrams are provided in the figure. In Fig. 5(b), the structure of the extensor mechanism was highly replicated on the reticular extensor, of which the RI, LE, and UI tendons are connected with each other through the tendon branches. In contrast, the RI, LE, and UI tendons are separated on the linear extensor, and the finger can be extended by only the LE tendon.

Experiments were then conducted to find the influence of different extensor morphologies on the feasible force space. Similar to the theoretical analysis, three postures of the two robotic fingers were tested. To obtain the fingertip feasible force space, a method similar to the one used in Valero-Cuevas [62] was adopted. As shown in Fig. 5(c) and (d), the robotic finger was actuated by five Dynamixel MX-12 W motors to pull the RI, UI, FDP, LE, and FPS tendons, respectively, with 0.099-N · m output torques (to obtain 9-N tendon force with 11-mm drive radius). The 9-N tendon force was selected based on the motors' maximum working output torques and also in consideration of not damaging the finger model. Only one tendon was pulled at a time, and the other tendons were in a rest state so that the fingertip force output contributed by each tendon can be separately recorded. In addition, a force-sensing resistor FSR-402 (Interlink Electronics, US) with 0.1-N resolution and 10-N maximum force range was used to obtain the fingertip force. The sensor was integrated with an Arduino Nano Every board and a liquid crystal display (LCD). It was placed near the fingertip and fixed on a plate that was perpendicular to the palmar (position 1) / distal (position 2) / radial (position 3) direction for collecting force data in these three directions. During the experiment, the force sensor was first placed in position 1, and one tendon of the robotic finger was pulled by the corresponding motor. The fingertip force was then read from the force sensor screen. After all the five tendons were tested, we moved the force sensor to position 2 and then position 3, and repeated the tests until the experiments were conducted in all the three directions (palmar, distal, and radial). Each tendon can generate one fingertip force composite space vector, and therefore, five fingertip force vectors of the robotic finger with the reticular extensor were obtained from the above

tests. The same experimental procedures were then conducted on the robotic finger with the linear extensor.

Using the minksum and convhull functions embedded in Matlab, the feasible output force space can be directly generated. Consequently, the comparison results of the physical model with reticular and linear extensors are presented in Fig. 6(g)–(i). The feasible force space of the physical model with a reticular extensor (the blue block) is relatively greater than that of the physical model with a linear extensor (the red block). The feasible force space volume results can be found in Table I. In terms of the experimental results, it is evident that the reticular extensor mechanism can significantly enlarge the fingertip feasible force space compared with the linear extensor structure in all three postures, of which the improvement percentage is 100.8% for posture 1, 80.7% for posture 2, and 257.7% for posture 3, showing 146.4% improvement on average. Compared with the theoretical results, the improvement in the experimental results is much more significant. Besides, the mathematical model results are much greater than the corresponding physical model results in all three postures. This is possibly due to the friction in the transmission system of the finger prototype and the errors from the joint moment arm and fingertip force measurement.

VI. Discussions

Researchers have been struggling to develop a robotic hand that can show comparable performance to the human hand. By carefully studying the musculoskeletal system of the human finger, this article developed a novel multilayer anthropomorphic robotic finger and theoretically and experimentally studied three human-finger-like biomechanical advantages embodied in the proposed robotic finger, shedding light on the better design of robotic fingers and hands.

A. Biomechanical Advantages

In Part I, two biomechanical advantages embedded in the ligamentous joint and the extensor mechanism were investigated through mathematical modeling and experimental verification.

Anisotropic variable stiffness of the ligamentous joint is one of the unique features of human fingers. Indeed, coping with a variety of daily activities requires different joint stiffness conditions. Low joint stiffness in small flexion angles endows the finger with good dexterity. In this condition, fingers can reach a large range of positions, enabling the hand to easily grasp objects with various sizes and shapes as well as complete some elaborate manipulations. On the other hand, high joint stiffness in large flexion angles can make fingers capable of bearing or resisting large lateral forces with reduced forces needed from the intrinsic muscles, e.g., pulling a rope or pinching a key [17]. In this article, with the mathematical modeling, prototype development, and experimental investigation, we have indicated that the variable stiffness property in the human finger joint can be achieved in the robotic finger through the proper design and careful selection of materials for the ligamentous structure. The joint stiffness varies and presents different variation characteristics in the flexion–extension and abduction–adduction directions, favoring the dexterity and stability demands in different directions. The proposed method can be further used to analyze the properties of other ligamentous joints. In addition, compared with the approach of cadaveric tests for studying the biomechanics of the hand [1], [14], [15], using a highly biomimetic robotic hand that contains the proposed bioinspired robotic fingers could make the related tests more economical and easier to be prepared and repeated.

Enlarged feasible force space is another biomechanical advantage achieved in the proposed robotic finger through the in-depth understanding [65], [66] and biomimetic design of the extensor mechanism. The enlarged fingertip feasible force space contributes to the practical performance by allowing exerting sufficient forces in any direction within the finger's workspace. This optimized mechanical output in the finger is particularly important when it interacts with the uncertain, unstructured, and irregular environment since various forces in any directions could be potentially required. The results from this article provide strong and intuitive evidence for the biomechanical advantage existing in the extensor mechanism of human fingers [23], [24].

B. Limitation and Future Work

Current design of the robotic finger only tried to employ the necessary structural elements similar to the human finger. To make the robotic finger better embody human-finger-like properties and functions, more detailed structures of the human finger should be considered, such as lumbrical muscle, accessory collateral ligament, joint cavity filled with the synovial fluid, etc. Besides, the current fabrication approach and the materials used could be optimized to improve the similarities between the designed elements and their corresponding structures in the human finger, such as using more types of fiber materials and proper weaving or knitting methods to fabricate the ligament, the joint capsule, and the extensor mechanism. These will be well considered in the future bioinspired robotic hand development of this research.

Moreover, the simplified mathematical models of the biological joint limit the accuracy of the theoretical analysis, which can be improved through computational modeling. In the experimental study, the press force sensor used in the feasible force space test could have been replaced by the six-axis force sensor to collect the force data in 3-D space at a single time, making the test more efficient.

VII. Conclusion

Based on a bioinspired robotic finger, this article for the first time systematically investigated three intrinsic biomechanical advantages in a human finger that can be embodied in robotic fingers. In Part I, through the investigation of the musculoskeletal system of human fingers, a multilayer anthropomorphic robotic finger was designed and developed. The proposed finger approximately embodies the morphological structures and the material properties of a human finger. It contains CT-scanned and 3-D printed bone models, PTFE-covered articular cartilages, PET braided fiber ligaments, silicone rubber joint capsules with wrinkles, silicone rubber tendon sheaths with PTFE tubes, and

polyester fishing line tendons. Based on this robotic finger, in this part, two human-finger-like biomechanical advantages were systematically explored through both mathematical modeling and experimental verification. Both geometrical and analytical approaches were used to characterize the influence of the ligamentous structure on the joint stiffness. Vector and matrix methods were employed to describe the impact of the reticular extensor on the fingertip feasible force space. The theoretical results were then verified by the experiments. The results have shown that biomechanical advantages of the anisotropic variable joint stiffness and the enlarged fingertip feasible force space could be achieved by the biomimetic design of the robotic finger. Grasping tests and comparisons are presented in Part II of this article, providing the indication of the biomechanical advantages investigated in this article.

APPENDIX A
FORWARD KINEMATIC MODEL AND THE JACOBIAN MATRIX OF THE ROBOTIC AND HUMAN FINGER

Substituting the structure parameters of the robotic finger into (37), $\mathbf{J}(\boldsymbol{q})^{-T}$ can be calculated as

$$\mathbf{J}(\boldsymbol{q})^{-T} = \begin{pmatrix} 1.78\times10^{-15} & -38.760 & 38.760 & 0 \\ 31.153 & -70.033 & 38.880 & 0 \\ 0 & 0 & 0 & 34.247 \\ 0.090 & -0.847 & 1.756 & 0 \end{pmatrix}. \tag{41}$$

For the human index finger, the structure parameters can be obtained from [2] and identified as $l_1 = 0.05$ m, $l_2 = 0.031$ m, $l_3 = 0.016$ m, $q_1 = \pi/4$, $q_2 = \pi/4$, $q_3 = \pi/18$, and $q_4 = 0$. Then, we can get $\mathbf{J}(\boldsymbol{q})^{-T}$ of the human finger, which is shown in

$$\mathbf{J}(\boldsymbol{q})^{-T} = \begin{pmatrix} 7.196\times10^{-15} & -32.258 & 32.258 & 0 \\ 28.284 & -60.542 & 32.258 & 0 \\ 0 & 0 & 0 & 30.697 \\ 0.079 & -0.677 & 1.598 & 0 \end{pmatrix}. \tag{42}$$

APPENDIX B
MOMENT ARM MATRIX CALCULATION BASED ON THE TEST OF THE RELATIONSHIP BETWEEN THE TENDON EXCURSION AND THE JOINT ANGLE

A testbed was constructed to obtain the relationship between the tendon excursion and the joint angle. The robotic finger was mounted on the testbed with its flexion–extension plane perpendicular to the floor. At the end of each muscle tendon, there is a 500-g load fixed through a pulley to straighten the tendon and keep it under constant tension during the whole joint motion. The test was conducted by passively moving each finger joint individually with the other joints maintained at a neutral position. At each step of the test, the joint was moved by a small angle. The joint angle and the excursion of each tendon (the descent distance of each load) were captured by a camera and obtained through the image processing in the software ImageJ.

Then, the experimental data of the tendon excursion was fitted by a three-order polynomial function and the result of the corresponding moment arm can be obtained from the derivative of the tendon excursion-joint angle curve.

TABLE II
MOMENT ARM OF EACH MUSCLE TENDON TO EACH JOINT IN THE STANDARD POSTURE OF THE ROBOTIC INDEX FINGER WITH THE RETICULAR EXTENSOR (MM)

Tendon	Joint angle (°)			
	DIP 10°	PIP 45°	MCP FL 45°	MCP ABD 0°
RI	0.47	-0.42	7.42	5.98
UI	1.52	0.23	7.04	-5.32
FDP	4.67	10.93	12.42	-2.22
LE	-1.26	-5.84	-10.79	1.05
FDS	0	8.79	9.57	-1.84

According to the coordinate definition, the flexion and abduction angles were set to be positive. And the moment arm of each tendon to the finger joint was listed in Table II, with the minus sign meaning the muscles contribute the negative torques to the joint angle increasing.

With the numbering definition of each joint and tendon in Section V, the moment arm matrix $\mathbf{R}^3{}_r(\boldsymbol{q})$ of the robotic finger with the reticular extensor in posture 3 can be directly derived from Table II

$$\mathbf{R}^3{}_r(\boldsymbol{q}) = \begin{pmatrix} 7.42 & 7.04 & 12.42 & -10.79 & 9.57 \\ -0.42 & 0.23 & 10.93 & -5.84 & 8.79 \\ 0.47 & 1.52 & 4.67 & -1.26 & 0 \\ 5.98 & -5.32 & -2.22 & 1.05 & -1.84 \end{pmatrix}. \tag{43}$$

Likewise, the moment arm matrix of the robotic finger in posture 1 (DIP at 5°, PIP at 15°, MCP flexion at 40°, and abduction at 0°) and posture 2 (DIP at 15°, PIP at 60°, MCP flexion at 80°, and abduction at 0°) can be identified as $\mathbf{R}^1{}_r(\boldsymbol{q})$ in (44) and $\mathbf{R}^2{}_r(\boldsymbol{q})$ in (45), respectively

$$\mathbf{R}^1{}_r(\boldsymbol{q}) = \begin{pmatrix} 7.63 & 6.74 & 11.68 & -10.54 & 9.24 \\ 1.88 & 0.12 & 10.75 & -7.59 & 8.63 \\ 0.79 & 1.98 & 4.24 & -1.47 & 0 \\ 5.98 & -5.32 & -2.22 & 1.05 & -1.84 \end{pmatrix} \tag{44}$$

$$\mathbf{R}^2{}_r(\boldsymbol{q}) = \begin{pmatrix} 4.10 & 3.91 & 15.44 & -11.77 & 13.22 \\ -2.72 & -0.90 & 11.77 & -4.96 & 8.14 \\ 0.12 & 1.05 & 5.09 & -1.05 & 0 \\ 5.98 & -5.32 & -2.22 & 1.05 & -1.84 \end{pmatrix}. \tag{45}$$

Besides, for the robotic finger with the linear extensor, the corresponding moment arm matrixes can be obtained in the same method as above. As a result, the moment arm matrixes in all the three postures are

$$\mathbf{R}^1{}_l(\boldsymbol{q}) = \begin{pmatrix} 6.58 & 5.66 & 12.33 & -10.31 & 9.15 \\ 0 & 0 & 10.36 & -6.81 & 8.32 \\ 0 & 0 & 4.73 & -1.27 & 0 \\ 6.6 & -4.09 & -2.04 & 1.64 & -2.03 \end{pmatrix} \tag{46}$$

$$\mathbf{R}^2{}_l(\boldsymbol{q}) = \begin{pmatrix} 3.32 & 3.28 & 15.7 & -12.02 & 14.0 \\ 0 & 0 & 10.14 & -3.42 & 8.15 \\ 0 & 0 & 4.74 & -1.01 & 0 \\ 6.6 & -4.09 & -2.04 & 1.64 & -2.03 \end{pmatrix} \tag{47}$$

$$\mathbf{R}^3{}_l(\boldsymbol{q}) = \begin{pmatrix} 6.77 & 5.92 & 12.63 & -10.59 & 10.15 \\ 0 & 0 & 9.91 & -5.08 & 9.02 \\ 0 & 0 & 4.70 & -1.04 & 0 \\ 6.6 & -4.09 & -2.04 & 1.64 & -2.03 \end{pmatrix}. \tag{48}$$

In addition, for the human index finger, the moment arm parameters in standard posture can be found in [2] and [64], and thus, the moment arm matrix $\mathbf{R}^h(\boldsymbol{q})$ of the human index finger is

$$\mathbf{R}^h(\boldsymbol{q}) = \begin{pmatrix} 2.00 & 4.00 & 12.00 & -7.77 & 13.20 \\ 0 & -2.75 & 6.50 & -2.75 & 5.85 \\ 0 & -1.50 & 3.64 & -1.50 & 0 \\ 6.77 & -4.08 & -2.90 & 1.19 & -1.45 \end{pmatrix}. \tag{49}$$

APPENDIX C
CALCULATION OF THE GENERATORS FOR THE FEASIBLE FORCE SPACE OF THE ROBOTIC AND HUMAN FINGER

The derivation equation of the fingertip output wrench is shown in (40), which can also be expressed as

$$\begin{pmatrix} \boldsymbol{f}_x \\ \boldsymbol{f}_y \\ \boldsymbol{f}_z \\ \boldsymbol{\tau}_z \end{pmatrix} = \begin{bmatrix} \boldsymbol{w}_1 & \boldsymbol{w}_2 & \boldsymbol{w}_3 & \boldsymbol{w}_4 & \boldsymbol{w}_5 \end{bmatrix} \begin{pmatrix} a_1 \\ a_2 \\ a_3 \\ a_4 \\ a_5 \end{pmatrix}. \tag{50}$$

In (50), the column vectors $\boldsymbol{w}_i$ are the generators of the Minkowski sum for the feasible force set. Each generator $\boldsymbol{w}_i$ is the force vector that the muscle i produces in space.

To clearly demonstrate the 3-D force generation capabilities of the fingertip, we can enforce the fingertip torque τ_z to be zero. Then, in the condition of 9-N maximum tendon force, with (41), (43), (40), and (50), the feasible force space generators of the robotic finger $\boldsymbol{w'}_i$ can be calculated as (51). And for the human index finger, the generators $\boldsymbol{w}^{h'}_i$ can be obtained with the same derivation process including (42), (44), (40), and (50), showing the results as

$$\begin{aligned} \boldsymbol{w'}_1 &= (0.311, 2.504, 1.841) \\ \boldsymbol{w'}_2 &= (0.450, 2.355, -1.638) \\ \boldsymbol{w'}_3 &= (-2.184, -1.767, -0.683) \\ \boldsymbol{w'}_4 &= (1.598, 0.213, 0.323) \\ \boldsymbol{w'}_5 &= (-3.066, -2.848, -0.566) \\ \boldsymbol{w}^{h'}{}_1 &= (1.599 \times 10^{-17}, 0.509, 1.870) \\ \boldsymbol{w}^{h'}{}_2 &= (0.363, 2.081, -1.127) \\ \boldsymbol{w}^{h'}{}_3 &= (-0.830, 0.570, -0.801) \\ \boldsymbol{w}^{h'}{}_4 &= (0.363, -0.915, 0.329) \\ \boldsymbol{w}^{h'}{}_5 &= (-1.698, 0.173, -0.401). \end{aligned} \tag{51, 52}$$

ACKNOWLEDGMENT

The authors would like to thank D. P. Connor, A. R. J. Dunbar, H. Yang, and L. Yan for assisting 3-D printing of the parts, and Y. Wei and B. Zhou for their insight and discussion throughout this work.

REFERENCES

[1] E. Y. Chao, *Biomechanics of the Hand: A Basic Research Study*. Singapore: World Scientific, 1989.
[2] F. J. Valero-Cuevas, F. E. Zajac, and C. G. Burgar, "Large index-fingertip forces are produced by subject-independent patterns of muscle excitation," *J. Biomech.*, vol. 31, no. 8, pp. 693–703, 1998.
[3] F. J. Valero-Cuevas, "A mathematical approach to the mechanical capabilities of limbs and fingers," in *Progress in Motor Control*. Berlin, Germany: Springer, 2009, pp. 619–633.
[4] P. W. Brand and A. Hollister, *Clinical Mechanics of the Hand*. St. Louis, MO, USA: Mosby Incorporated, 1999.
[5] R. Pfeifer, M. Lungarella, and F. Iida, "Self-organization, embodiment, and biologically inspired robotics," *Science*, vol. 318, no. 5853, pp. 1088–1093, 2007.
[6] R. Pfeifer, M. Lungarella, and F. Iida, "The challenges ahead for bio-inspired 'soft' robotics," *Commun. ACM*, vol. 55, no. 11, pp. 76–87, 2012.
[7] A. D. Deshpande et al., "Mechanisms of the anatomically correct testbed hand," *IEEE/ASME Trans. Mechatronics*, vol. 18, no. 1, pp. 238–250, Feb. 2013.
[8] J. Hughes, P. Maiolino, and F. Iida, "An anthropomorphic soft skeleton hand exploiting conditional models for piano playing," *Sci. Robot.*, vol. 3, no. 25, 2018, Art. no. aau3098.
[9] M. Chepisheva, U. Culha, and F. Iida, "A biologically inspired soft robotic hand using chopsticks for grasping tasks," in *Proc. Int. Conf. Simul. Adaptive Behav.*, 2016, pp. 195–206.
[10] M. Tebyani et al., "3D printing an assembled biomimetic robotic finger," in *Proc. 17th Int. Conf. Ubiquitous Robots*, 2020, pp. 526–532.
[11] A. B. Leger and T. E. Milner, "Passive and active wrist joint stiffness following eccentric exercise," *Eur. J. Appl. Physiol.*, vol. 82, no. 5, pp. 472–479, 2000.
[12] N. Miyamoto, K. Hirata, E. Miyamoto-Mikami, O. Yasuda, and H. Kanehisa, "Associations of passive muscle stiffness, muscle stretch tolerance, and muscle slack angle with range of motion: Individual and sex differences," *Sci. Rep.*, vol. 8, no. 1, pp. 1–10, 2018.
[13] P.-H. Kuo and A. D. Deshpande, "Muscle-tendon units provide limited contributions to the passive stiffness of the index finger metacarpophalangeal joint," *J. Biomech.*, vol. 45, no. 15, pp. 2531–2538, 2012.
[14] D. Werner, S. H. Kozin, M. Brozovich, S. T. Porter, D. Junkin, and S. Seigler, "The biomechanical properties of the finger metacarpophalangeal joints to varus and valgus stress," *J. Hand Surg.*, vol. 28, no. 6, pp. 1044–1051, 2003.
[15] K. Lutsky, J. Matzon, L. Walinchus, D. A. Ross, and P. Beredjiklian, "Collateral ligament laxity of the finger metacarpophalangeal joints: An in vivo study," *J. Hand Surg.*, vol. 39, no. 6, pp. 1088–1093, 2014.
[16] T. Kataoka, H. Moritomo, J. Miyake, T. Murase, H. Yoshikawa, and K. Sugamoto, "Changes in shape and length of the collateral and accessory collateral ligaments of the metacarpophalangeal joint during flexion," *J. Bone Joint Surg.*, vol. 93, no. 14, pp. 1318–1325, 2011.
[17] M. Grebenstein, "Approaching human performance: The functionality-driven Awiwi robot hand," *Springer Tracts Adv. Robot.*, vol. 98, Springer, Cham., 2014.
[18] Z. Xu and E. Todorov, "Design of a highly biomimetic anthropomorphic robotic hand towards artificial limb regeneration," in *Proc. IEEE Int. Conf. Robot. Automat.*, 2016, pp. 3485–3492.
[19] F. J. Valero-Cuevas, "Predictive modulation of muscle coordination pattern magnitude scales fingertip force magnitude over the voluntary range," *J. Neuriophysiol.*, vol. 83, no. 3, pp. 1469–1479, 2000.
[20] F. J. Valero-Cuevas, "An integrative approach to the biomechanical function and neuromuscular control of the fingers," *J. Biomech.*, vol. 38, no. 4, pp. 673–684, 2005.

[21] J. M. Inouye, J. J. Kutch, and F. J. Valero-Cuevas, "A novel synthesis of computational approaches enables optimization of grasp quality of tendon-driven hands," *IEEE Trans. Robot.*, vol. 28, no. 4, pp. 958–966, Aug. 2012.

[22] S. Shirafuji, S. Ikemoto, and K. Hosoda, "Development of a tendon-driven robotic finger for an anthropomorphic robotic hand," *Int. J. Robot. Res.*, vol. 33, no. 5, pp. 677–693, 2014.

[23] F. J. Valero-Cuevas, J.-W. Yi, D. Brown, R. V. McNamara, C. Paul, and H. Lipson, "The tendon network of the fingers performs anatomical computation at a macroscopic scale," *IEEE Trans. Biomed. Eng.*, vol. 54, no. 6, pp. 1161–1166, Jun. 2007.

[24] A. Synek and D. H. Pahr, "The effect of the extensor mechanism on maximum isometric fingertip forces: A numerical study on the index finger," *J. Biomech.*, vol. 49, no. 14, pp. 3423–3429, 2016.

[25] F. J. Valero-Cuevas, J. D. Towles, and V. R. Hentz, "Quantification of fingertip force reduction in the forefinger following simulated paralysis of extensor and intrinsic muscles," *J. Biomech.*, vol. 33, no. 12, pp. 1601–1609, 2000.

[26] F. J. Valero-Cuevas and H. Lipson, "A computational environment to simulate complex tendinous topologies," in *Proc. 26th Annu. Int. Conf. IEEE Eng. Med. Biol. Soc.*, 2004, vol. 2, pp. 4653–4656.

[27] D. D. Wilkinson, M. V. Weghe, and Y. Matsuoka, "An extensor mechanism for an anatomical robotic hand," in *Proc. IEEE Int. Conf. Robot. Automat. (Cat. No 03CH37422)*, 2003, vol. 1, pp. 238–243.

[28] A. D. Deshpande, R. Balasubramanian, J. Ko, and Y. Matsuoka, "Acquiring variable moment arms for index finger using a robotic testbed," *IEEE Trans. Biomed. Eng.*, vol. 57, no. 8, pp. 2034–2044, Aug. 2010.

[29] A. Leo, G. Handjaras, H. Marino, M. Bianchi, P. Pietrini, and E. Ricciardi, *Human and Robot Hands: Sensorimotor Synergies to Bridge the Gap Between Neuroscience and Robotics*, vol. 1. Berlin, Germany: Springer, 2016.

[30] S. C. Jacobsen, J. E. Wood, D. F. Knutti, and K. B. Biggers, "The UTAH/MIT dextrous hand: Work in progress," *Int. J. Robot. Res.*, vol. 3, no. 4, pp. 21–50, 1984.

[31] G. A. Bekey, R. Tomovic, and I. Zeljkovic, "Control architecture for the Belgrade/USC hand," in *Dextrous Robot Hands*. Berlin, Germany: Springer, 1990, pp. 136–149.

[32] P. J. Kyberd, C. Light, P. H. Chappell, J. M. Nightingale, D. Whatley, and M. Evans, "The design of anthropomorphic prosthetic hands: A study of the Southampton Hand," *Robotica*, vol. 19, no. 6, pp. 593–600, 2001.

[33] T. Mouri, H. Kawasaki, K. Yoshikawa, J. Takai, and S. Ito, "Anthropomorphic robot hand: Gifu hand III," in *Proc. Int. Conf. Control, Automat., Syst.*, 2002, pp. 1288–1293.

[34] M. C. Carrozza, G. Cappiello, S. Micera, B. B. Edin, L. Beccai, and C. Cipriani, "Design of a cybernetic hand for perception and action," *Biol. Cybern.*, vol. 95, no. 6, pp. 629–644, 2006.

[35] H. Liu et al., "Multisensory five-finger dexterous hand: The DLR/HIT hand II," in *Proc. IEEE/RSJ Int. Conf. Intell. Robots Syst.*, 2008, pp. 3692–3697.

[36] L. B. Bridgwater et al., "The Robonaut 2 hand-designed to do work with tools," in *Proc. IEEE Int. Conf. Robot. Automat.*, 2012, pp. 3425–3430.

[37] "Shadow dexterous hand technical specification," Feb. 2019, Accessed: Jun. 5, 2021. [Online]. Available: https://www.shadowrobot.com/dexterous-hand-series/

[38] J. S. Dai and D. Wang, "Geometric analysis and synthesis of the metamorphic robotic hand," *J. Mech. Des.*, vol. 129, no. 11, pp. 1191–1197, 2007.

[39] E. Emmanouil, G. Wei, and J. S. Dai, "Spherical trigonometry constrained kinematics for a dexterous robotic hand with an articulated palm," *Robotica*, vol. 34, no. 12, pp. 2788–2805, 2017.

[40] R. Deimel and O. Brock, "A novel type of compliant and underactuated robotic hand for dexterous grasping," *Int. J. Robot. Res.*, vol. 35, no. 1–3, pp. 161–185, 2016.

[41] F. Lotti, P. Tiezzi, G. Vassura, L. Biagiotti, G. Palli, and C. Melchiorri, "Development of UB Hand 3: Early results," in *Proc. IEEE Int. Conf. Robot. Automat.*, 2005, pp. 4488–4493.

[42] G. P. Kontoudis, M. V. Liarokapis, A. G. Zisimatos, C. I. Mavrogiannis, and K. J. Kyriakopoulos, "Open-source, anthropomorphic, underactuated robot hands with a selectively lockable differential mechanism: Towards affordable prostheses," in *Proc. IEEE/RSJ Int. Conf. Intell. Robots Syst.*, 2015, pp. 5857–5862.

[43] A. A. M. Faudzi, J. Ooga, T. Goto, M. Takeichi, and K. Suzumori, "Index finger of a human-like robotic hand using thin soft muscles," *IEEE Robot. Automat. Lett.*, vol. 3, no. 1, pp. 92–99, Jan. 2018.

[44] D. A. Neumann, *Kinesiology of the Musculoskeletal System: Foundation for Rehabilitation*. St. Louis, MO, USA: Mosby & Elsevier, 2010.

[45] Y. Wei, Z. Zou, G. Wei, L. Ren, and Z. Qian, "Subject-specific finite element modelling of the human hand complex: Muscle-driven simulations and experimental validation," *Ann. Biomed. Eng.*, vol. 48, pp. 1181–1195, 2020.

[46] M. Nordin, V. H. Frankel, and D. Leger, *Basic Biomechanics of the Musculoskeletal System*. Baltimore, MD, USA: Wolters Kluwer/Lippincott Williams & Wilkins Health, 2012.

[47] T. Ogura et al., "Sat0661 finger joint cartilage thickness evaluated by ultrasound in patients with rheumatoid arthritis (RA)," *Ann. Rheumatic Dis.*, vol. 76, no. Suppl 2, pp. 1024–1025, 2017.

[48] C. Wan, Z. Hao, and S. Wen, "A review on research on development of ligament constitutive relations on Macro, Meso, and Micro levels," *Acta Mechanica Solida Sinica*, vol. 26, no. 4, pp. 331–343, 2013.

[49] J. R. Ralphs and M. Benjamin, "The joint capsule: Structure, composition, ageing and disease," *J. Anatomy*, vol. 184, no. Pt3, pp. 503–509, 1994.

[50] J. Watkins, *Pocket Podiatry: Functional Anatomy*. Amsterdam, The Netherlands: Elsevier Health Sciences, 2009.

[51] J. C. Thompson and F. Netter, *Netter's Concise Atlas of Orthopaedic Anatomy*, 1st ed., Philadelphia, PA, USA: Saunders, 2002.

[52] E. Zancolli, *Structural and Dynamic Bases of Hand Surgery*. Philadelphia, PA, USA: Lippincott Williams & Wilkins, 1979.

[53] H. J. Goodman and J. Choueka, "Biomechanics of the flexor tendons," *Hand Clin.*, vol. 21, no. 2, pp. 129–149, 2005.

[54] J. R. Doyle and M. J. Botte, *Surgical Anatomy of the Hand and Upper Extremity*. Philadelphia, PA, USA: Lippincott Williams & Wilkins, 2003.

[55] C. A. Oatis, *Kinesiology: The Mechanics and Pathomechanics of Human Movement*, 2nd ed. Philadelphia, PA, USA: Lippincott Williams & Wilkins, 2008.

[56] I. Komatsu and J. D. Lubahn, "Anatomy and biomechanics of the thumb carpometacarpal joint," *Operative Techn. Orthopaedics*, vol. 28, no. 1, pp. 1–5, 2018.

[57] P. C. Bettinger, R. L. Linscheid, R. A. Berger, W. P. Cooney, and K.-N. An, "An anatomic study of the stabilizing ligaments of the trapezium and trapeziometacarpal joint," *J. Hand Surg.*, vol. 24, no. 4, pp. 786–798, 1999.

[58] M. Nanno, W. L. Buford, R. M. Patterson, C. R. Andersen, and S. F. Viegas, "Three-dimensional analysis of the ligamentous attachments of the first carpometacarpal joint," *J. Hand Surg.*, vol. 31, no. 7, pp. 1160–1170, 2006.

[59] A. L. Ladd, J. Lee, and E. Hagert, "Macroscopic and microscopic analysis of the thumb carpometacarpal ligaments: A cadaveric study of ligament anatomy and histology," *J. Bone Joint Surg. Amer.*, vol. 94, no. 16, pp. 1468–1477, 2012.

[60] W. P. Smutz, A. Kongsayreepong, R. E. Hughes, G. Niebur, W. P. Cooney, and K.-N. An, "Mechanical advantage of the thumb muscles," *J. Biomech.*, vol. 31, no. 6, pp. 565–570, 1998.

[61] R. M. Alexander and M. B. Bennett, "Some principles of ligament function, with examples from the tarsal joints of the sheep (Ovis aries)," *J. Zool.*, vol. 211, no. 3, pp. 487–504, 1987.

[62] F. J. Valero-Cuevas, *Fundamentals of Neuromechanics*. Berlin, Germany: Springer, 2016.

[63] F. J. Valero-Cuevas and V. R. Hentz, "Releasing the A3 pulley and leaving flexor superficialis intact increases pinch force following the Zancolli lasso procedures to prevent claw deformity in the intrinsic palsied finger," *J. Orthopaedic Res.*, vol. 20, no. 5, pp. 902–909, 2002.

[64] K.-N. An, Y. Ueba, E. Y. Chao, W. P. Cooney, and R. L. Linscheid, "Tendon excursion and moment arm of index finger muscles," *J. Biomech.*, vol. 16, no. 6, pp. 419–425, 1983.

[65] D. Hu, L. Ren, D. Howard, and C. Zong, "Biomechanical analysis of force distribution in human finger extensor mechanisms," *BioMed Res. Int.*, vol. 2014, 2014, Art. no. 743460.

[66] D. Hu, D. Howard, and L. Ren, "Biomechanical analysis of the human finger extensor mechanism during isometric pressing," *PLoS One*, vol. 9, no. 4, 2014, Art. no. e94533.

[67] J. Inouye and F. J. Valero-Cuevas, "Asymmetric routings with fewer tendons can offer both flexible endpoint stiffness control and high force-production capabilities in robotic fingers," in *Proc. 4th IEEE RAS EMBS Int. Conf. Biomed. Robot. Biomechatronics*, 2012, pp. 1273–1280.

[68] J. S. Dai, D. Wang, and L. Cui, "Orientation and workspace analysis of the multifingered metamorphic hand-metahand," *IEEE Trans. Robot.*, vol. 25, no. 4, pp. 942–947, Aug. 2009.

[69] G. Wei, J. S. Dai, S. Wang, and H. Luo, "Kinematic analysis and prototype of a metamorphic anthropomorphic hand with a reconfigurable palm," *Int. J. Humanoid Robot.*, vol. 8, no. 3, pp. 459–479, 2011.

Yiming Zhu received the Ph.D. degree in mechanical engineering from the University of Manchester, Manchester, U.K., in 2021.

He is currently a Lecturer of Intelligence Mechanics with the College of Intelligence Science and Technology, National University of Defense Technology, Changsha, China. His research interests include biorobotics and biomechanics, particularly the biomimetic robotic hand development.

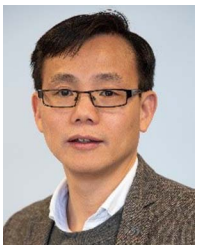

Guowu Wei (Member, IEEE) received the Ph.D. degree in robotics from King's College London, London, U.K., in 2012.

He is currently a Lecturer of Robotics and Mechanical Engineering with the School of Science, Engineering and Environment, University of Salford, Salford, U.K. He has more than 120 peer-reviewed publications. His research was funded by EPSRC, EU-FP7, ICUK, NSFC, and Royal Academy of Engineering. His research interests include robotics, mechatronics, and manipulation and grasping, reconfigurable mechanisms and robotics, and biorobotics.

Dr. Wei is the Associate Editor for *Robotica* and *Journal of Mechanical Engineering Science*, the Topic Editor for *Mechanical Science*, the Academic Editor for *Applied Bionics and Biomechanics*, and the Associate Editor for the IEEE/RSJ International Conference on Intelligent Robots and Systems and IEEE International Conference on Robotics and Automation. He is currently the Deputy Chair of IFToMM MO U.K.

Lei Ren (Member, IEEE) received the Ph.D. degree in biomechanical engineering from the University of Salford, Manchester, U.K., in 2005.

He is currently the Leader of biomechanics specialism with Department of Mechanical, Aerospace, and Civil Engineering, University of Manchester and with the Key Laboratory of Bionic Engineering, Ministry of Education, Jilin University, Changchun, China. He has authored or coauthored more than 280 peer-reviewed publications and the holder of 120 patents. His research interests include the field of biorobotics and biomechanics, including humanoid locomotion, hand grasping and manipulation, and bioinspired limb prosthetics. His research works have been reported by Nature, Science News, Wired, Telegraph, Science Daily, and BBC.

Dr. Ren is currently the Deputy General Secretary of the International Society of Bionic Engineering, Nottingham, U.K. and with the Council of Chairs, Biomedical Engineering Society, Landover, MD, USA. He is an Associate Editor-in-Chief for *Journal of Bionic Engineering*, an Associate Editor for *Frontiers in Bioengineering and Biotechnology*, and the Editorial Member of *Frontiers of Mechanical Engineering, Journal of Healthcare Engineering*, and *Chinese Journal of Mechanical Engineering*. He was the Principle Investigator and the Co-Investigator of more than 30 research projects funded by Engineering and Physical Sciences Research Council, Biotechnology and Biological Sciences Research Council, National Natural Science Foundation of China, and MoST.

Zirong Luo received the Ph.D. degree in mechanical engineering from the National University of Defense Technology (NUDT), Changsha, China, in 2010.

He is currently a Professor of Mechanical Engineering with the College of Intelligence Science and Technology, NUDT. He has authored or coauthored more than 80 peer-reviewed publications and has been awarded more than 50 related patents. His current research interests include unmanned system, mobile robots, wave energy, bioinspired robots, and microrobots.

Jianzhong Shang received the Ph.D. degree in mechanical engineering from the Huazhong University of Science and Technology, Wuhan, China, in 2006.

He is currently a Professor and a Doctoral Supervisor with the College of Intelligence Science and Technology, National University of Defense Technology, Changsha, China. He researches in the field of mechanical engineering, including robotics, biomechanics, digital design, and manufacturing and has more than 100 peer-reviewed publications.

Dr. Shang is a recipient of the Second Prize of National Science and Technology Progress.